Colored dissolved organic matter (CDOM) alters the seasonal physics and biogeochemistry of the Arctic Mackenzie River plume

Clement Bertin¹, Vincent Le Fouest², Dustin Carroll^{3,1}, Stephanie Dutkiewicz⁴, Dimitris Menemenlis¹, Atsushi Matsuoka⁵, Manfredi Manizza^{6,7}, and Charles E. Miller¹

Correspondence: Clement Bertin (clement.maxime.bertin@jpl.nasa.gov)

Abstract. Arctic warming affects land-to-ocean fluxes of organic matter through increased permafrost thaw, coastal erosion or river discharge, with significant impacts on coastal ecosystems and air-sea CO₂ fluxes. In this study, we modify a regional version of the Estimating the Circulation and Climate of the Ocean model coupled to the Darwin ocean biogeochemistry module (ECCO-Darwin) to simulate Mackenzie River export of colored dissolved organic matter (CDOM) and its effect on light attenuation, marine carbon cycling, and water-column heating from UV-A to visible light absorption. We find that CDOM light attenuation triggers both a two-week delay in the seasonal phytoplankton bloom and an increase in sea-surface temperature (SST) by 1.7°C. While the change in phytoplankton phenology has limited effect on air-sea CO₂ fluxes, the local increase in SST due to terrestrial organic matter input switches the coastal zone from an annual sink of atmospheric CO₂ to a source (7.35 Gg C yr⁻¹). Our work suggests that the projected increase in terrestrial CDOM has strong implications for phytoplankton phenology and coastal air-sea carbon exchange in the Arctic.

1 Introduction

As anthropogenic emissions of carbon dioxide (CO_2) continue to increase (IPCC, 2023), it is critical to understand the time variability and future trajectory of the ocean carbon sink and its regional-scale response. The Arctic Ocean (AO) region constitutes an important sink of atmospheric CO_2 , estimated to be 116 ± 4 Tg C yr⁻¹ (Yasunaka et al., 2023), or roughly 7% of the global-ocean sink (Roobaert et al., 2019). When focusing on coastal regions, the AO contribution constitutes up to 46% of the global sink (Dai et al., 2022). The intense cooling of inflowing waters from adjacent seas and favorable conditions for phytoplankton growth result in elevated CO_2 uptake from increased CO_2 solubility and biological consumption, respectively. With Arctic air temperatures rising three to four time faster than the global mean due to the ice-albedo feedback (Rantanen et al., 2022), retreating sea ice cover allows for a larger ocean surface area to be exposed to sunlight for longer periods of time

¹Jet Propulsion Laboratory, California Institute of Technology, Pasadena, CA, USA

²LIttoral ENvironnement et Sociétés (LIENSs) – UMR 7266, Bâtiment ILE, 2 rue Olympe de Gouges, 17000 La Rochelle, France

³Moss Landing Marine Laboratories, San José State University, Moss Landing, CA, USA

⁴Department of Earth Atmospheric and Planetary Sciences, Massachusetts Institute of Technology, Cambridge, MA, USA

⁵Institute for the Study of Earth, Oceans, and Space, University of New Hampshire, Durham, USA

⁶Geosciences Research Division, Scripps Institution of Oceanography, University of California San Diego, La Jolla, USA

⁷Istituto Nazionale di Oceanografia e di Geofisica Sperimentale – OGS, Trieste, Italy

20 (Bliss et al., 2019; Ardyna and Arrigo, 2020). As a result, AO Net Primary Production (NPP) increased by 90 Tg C (38%) from 1998–2012 (Ardyna and Arrigo, 2020; Lewis et al., 2020). Additionally, recent work by Terhaar et al. (2021) showed that a third of AO primary production is sustained by terrestrial fluxes from coastal erosion and rivers, resulting from large lateral fluxes of carbon and nutrients (Dittmar and Kattner, 2003; Le Fouest et al., 2013; Nielsen et al., 2022). However, the quantity and the composition of terrestrial matter exported to coastal regions is also impacted by climate change (Bertin et al., 2022; Mann et al., 2022; Tank et al., 2023), with potential to affect the biophysical conditions of coastal AO waters.

As Arctic river freshwater discharge increases (Feng et al., 2021), the quantity of terrestrial dissolved organic matter (DOM) exported to AO coastal peripheries is expected to increase. Due to complex molecular composition including aromatic cycles, DOM chemical composition depends on its origin and encompasses more than 20,000 molecular formulae (Dittmar et al., 2021). As it transitions from land to ocean, microbial activity and light alter DOM molecules, with their chemical composition being highly dependent on the transit through the terrestrial-aquatic environment (Cory et al., 2014; Cory and Kling, 2018). Once in coastal waters, the composition of riverine-derived DOM varies seasonally, likely being more labile (i.e., more easily degraded by microbes) during spring freshet (Spencer et al., 2009). A fraction of DOM, termed colored DOM (CDOM), possesses unique optical characteristics that enable it to efficiently absorb shortwave radiation — from ultraviolet (UV) to the visible light spectrum. In Arctic rivers, CDOM molecular weight and aromaticity increases with discharge (Mann et al., 2016), rendering it more resistant to degradation by marine bacteria (i.e., more refractory). Simultaneously, its interaction with light transforms CDOM either into 1) more-labile components of DOM (Osburn et al., 2009; Cory and Kling, 2018) or 2) directly into Dissolved Inorganic Carbon (DIC; Bélanger et al., 2006; Aarnos et al., 2018), which can promote CO₂ outgassing. By dampening light penetration into the water column, CDOM can impact primary production (Li et al., 2024; Berezovski et al., 2025) and upper-ocean temperature (Hill, 2008; Kim et al., 2016; Soppa et al., 2019), which can also modulate air-sea CO₂ exchange. Consequently, air-sea CO₂ flux magnitude and direction in AO river plume regions remain highly uncertain, with both local-to-regional outgassing or uptake observed (Terhaar et al., 2019; Bertin et al., 2023; Roobaert et al., 2024). Additionally, as a result of global warming, accelerating permafrost thaw has the potential to change the composition of organic matter in coastal waters and therefore the coastal air-sea CO₂ fluxes via increased coastal erosion (Tanski et al., 2021; Nielsen et al., 2024) or river discharge (Mann et al., 2022). Thus, by a cascading effect, CDOM can locally amplify sea ice melting due to increased sea-surface temperature (SST) from increased light attenuation (Pefanis et al., 2020). Therefore, understanding how terrestrial CDOM biophysical feedbacks influence coastal waters is critical to better characterize the consequences of climate change across Arctic coastal peripheries.

In AO coastal regions, NPP remains highly uncertain. The harsh polar conditions make it challenging to collect in-situ observations and estimates from remote sensing are often contaminated by sea ice, clouds, low light levels, and the high proportion of CDOM light absorption (Lewis and Arrigo, 2020; Li et al., 2024). Estimating NPP remotely also requires several key assumptions regarding the vertical distribution of phytoplankton, since satellites only capture near-surface data (Arrigo et al., 2011; Silsbe et al., 2016). Current estimates suggest AO NPP ranges from 203–516 Tg C yr⁻¹ (Bélanger et al., 2013; Arrigo

and Van Dijken, 2015), but these values are likely overestimated in coastal regions due to high CDOM concentrations. As a result, satellite estimates of air-sea CO₂ flux often fail to capture nearshore, river-plume regions (Bertin et al., 2023). To complement remote sensing, ocean biogeochemistry models (OBMs) permit full space-time coverage of AO coastal regions and can provide a mechanistic understanding of the processes that govern the air-sea CO₂ flux (Manizza et al., 2019; Mathis et al., 2022). Yet while most regional-scale OBMs now incorporate land-to-ocean nutrient transport (Terhaar et al., 2019; Lacroix et al., 2021; Savelli et al., 2025), their representation of the intricacies due to the CDOM feedbacks described above often remains partial or completely absent (though see e.g. Kim et al., 2018; Gnanadesikan et al., 2019; Pefanis et al., 2020).

In this study, we utilize a regional ocean-sea-ice-biogeochemistry model (ECCO-Darwin) to examine how riverine CDOM impacts the seasonal cycle of phytoplankton biomass, primary productivity, and carbon cycling in the coastal AO. Our objectives are to 1) separate and explicitly quantify how CDOM's light attenuation properties affect both the physics and biogeochemistry in the river plume and 2) estimate how riverine CDOM modulates coastal air-sea CO₂ flux. Here, we focus on the Southeastern Beaufort Sea (SBS), where the Mackenzie River discharges substantial freshwater and DOM into the AO (Bertin et al., 2022; Juhls et al., 2022). The remainder of this paper is structured as follows. First, we describe improvements made to the existing ECCO-Darwin regional configuration of the Southeastern Beaufort Sea (ED-SBS) regional set-up (Run_{strat} in Bertin et al., 2025) to incorporate CDOM processes and add riverine CDOM forcing. Second, we analyze the seasonal biophysical conditions simulated by ED-SBS in the Mackenzie River plume. Third, we assess the impact of riverine CDOM on the physical characteristics of the plume region. Fourth, we analyze changes in phytoplankton phenology driven by riverine CDOM. Fifth, we estimate how CDOM impacts air-sea CO₂ flux within the plume region. Finally, we provide concluding remarks and suggestions for future work.

75 2 Methods

2.1 Explicit CDOM tracer parameterization

To simulate the coastal Arctic Ocean environment, we used the ED-SBS regional configuration, whose general numerical characteristics are fully detailed in Supporting Information Text S1 and in Bertin et al. (2023, 2025). ED-SBS explicitly simulated four plankton functional types (PFTs) representative of ecosystems in the AO (diatoms, large eukaryotes, and small and large zooplankton), along with phytoplankton Chl concentrations. Two marine dissolved organic carbon (DOC) pools are simulated with chemical properties representative of those found in the coastal AO: a semi-refractory pool (DOC $_{sr}$) characterizing the long-residence-time carbon loop with a lifetime of $\tau = 10$ years (Manizza et al., 2009), and a semi-labile pool (DOC $_{sl}$) characterizing the short-residence-time carbon loop with a lifetime of $\tau = 1$ month (including DOC molecules characterized by turnover rates ranging from weeks to months; Holmes et al., 2008; Spencer et al., 2015; Bertin et al., 2025). Land-to-sea forcing included daily discharge of freshwater and 6 biogeochemical tracers from the Mackenzie River, distributed over the three major Mackenzie Delta outlets: Shallow Bay (29.8%), Beluga Bay (37.6%), and Kugmallit Bay (32.6%) (Morley, 2012; Bertin et al., 2022). Freshwater discharge was driven by daily gauge measurements from the Arctic Great River Observatory

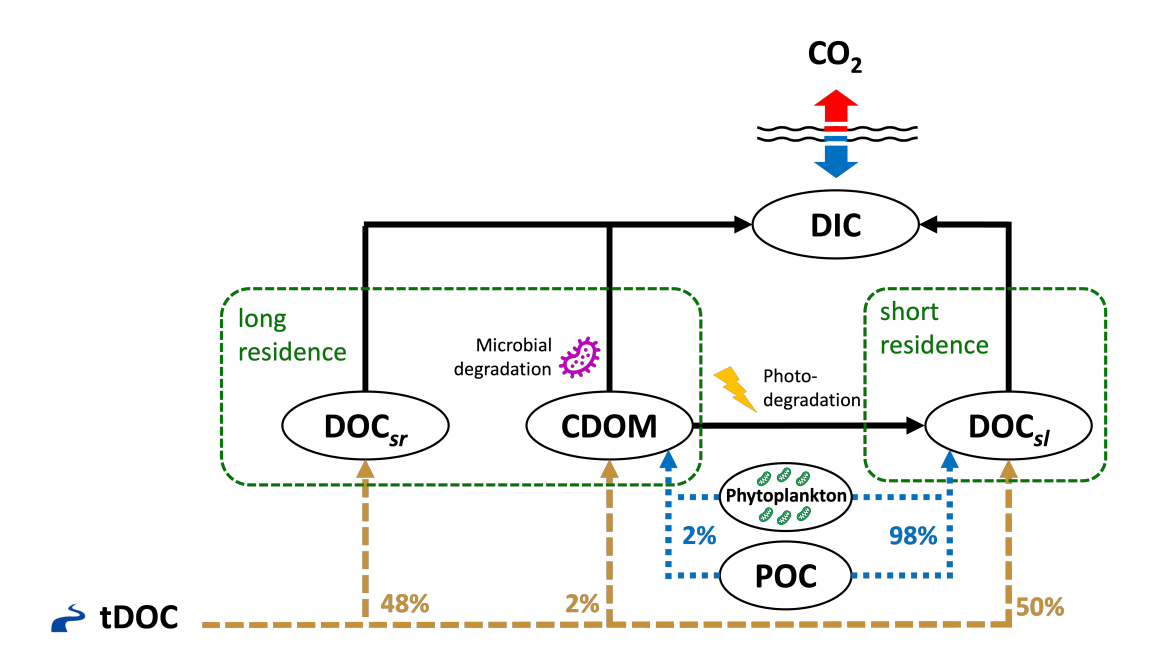


Figure 1. Conceptual diagram of dissolved carbon mass fluxes in the ED-SBS model. Mackenzie River terrestrial DOC (tDOC) mass flux (dashed brown lines) is distributed into marine DOC and CDOM pools according to the percentages shown in brown text. The result of phytoplankton grazing/mortality and particulate organic carbon (POC) dissolution is distributed over the DOC_{sl} and CDOM pools (dotted blue lines).

(ArcticGRO; McClelland et al., 2023) and was linked to daily river temperature obtained from the Tokuda et al. (2019) dataset. Riverine concentrations of DOC, dissolved organic nitrogen (DON), dissolved organic phosphorus (DOP), dissolved silicate (DSi), dissolved inorganic carbon (DIC), and alkalinity (Alk) were forced as detailed in Bertin et al. (2025). As each export of dissolved organic constituents (DOC, DON & DOP) are estimated independently, the terrestrial dissolved organic matter pool is not constrained by a constant C:N:P ratio (such as Terhaar et al., 2019; Gibson et al., 2022; Bertin et al., 2023).

In this study, we added an explicit "CDOM-like" tracer to ED-SBS, expressed as a carbon mass concentration (mmol C $\,\mathrm{m}^{-3}$), following the schematic shown in Figure 1. Terrestrial CDOM, which is observed to be non-labile (Blough and Del Vecchio, 2002; Aarnos et al., 2018), was added to the long-residence-time carbon loop of the model using the same microbial turnover time as DOC_{sr} ($\tau = 10$ years). The CDOM tracer also interacted with the short-residence-time carbon loop by photochemical alteration of CDOM into more-labile carbon (Ward et al., 2017; Grunert et al., 2021; Clark et al., 2022). CDOM was photodegraded into DOC_{sl} with a maximum bleaching turnover time of 6 days (Dutkiewicz et al., 2015), which was modulated by light intensity. Bleaching rate linearly increased from 0 when light intensity is 0 W m^{-2} to a maximum value (0.167 days $^{-1}$) when light is above 13 W m^{-2} (Dutkiewicz et al., 2015). CDOM photodegradation rate corresponds to the bleaching rate modulated by a temperature function. When degraded into DOC_{sl} , CDOM products DON and DOP following the Redfield

ratio of 120:16:1, allowing to represent the additional nutrient input generated by organic matter consumption — Redfield ratio is used due to a lack of data regarding CDOM photodegradation products. A fraction f_{CDOM} (= 2%) of mass fluxes received by DOC_{sl} through phytoplankton grazing/mortality and particulate organic carbon (POC) dissolution was also redistributed to CDOM.

In ED-SBS, Mackenzie River terrestrial DOC (tDOC) mass flux was equally distributed (50%) between semi-labile (DOC $_{sl}$) and semi-refractory (DOC $_{sr}$) DOC pools (based on recent estimates of the bioavailable tDOC fraction in the SBS, F. Joux, unpublished data from Nunataryuk field campaign; Tisserand et al., 2021; Lizotte et al., 2023). While 97% of DOC concentration variance is explained by CDOM absorption (Matsuoka et al., 2012), the mass concentration of riverine CDOM exported to SBS coastal waters remains unknown. As CDOM is part of the long-residence-time loop, we redistributed a percentage of tDOC mass flux from DOC $_{sr}$ into the CDOM pool. After a sensitivity analysis (detailed in Appendix B), we set the ratio to 2% — re-partitioning Mackenzie River tDOC mass flux into 50%, 48%, and 2% DOC $_{sl}$, DOC $_{sr}$, and CDOM, respectively. Our ratio of total tDOC exported as CDOM falls in the lower range of estimates for the top 10 DOC exporting rivers (4–38% of tDOC; Aarnos et al., 2018). Finally, we generated CDOM initial and boundary conditions following the methods detailed in Supporting Information Text S2.

2.2 CDOM light attenuation relationship

105

110

We first developed a new method for simulating CDOM light attenuation across the shortwave spectrum, from 320–735 nm. This allowed us to resolve the physical effect of CDOM light attenuation occurring in the UV-A (320–400 nm) and in the visible (400–735 nm) bands; the latter is often associated with Photosynthetically Active Radiation (PAR; spanning from 400–700 nm). An analysis of 31 CDOM spectral absorption measurements taken during the 2009 Malina campaign for different CDOM conditions across the SBS (see sampling locations in Supporting Information Figure S1; Matsuoka et al., 2012; Massicotte et al., 2021) revealed that 40%±10 (min:26–max:55) of light is absorbed by CDOM in the UV-A spectrum. These observations highlight the need to include full-band CDOM representation in OBMs, as most models only include light attenuation effects across PAR wavelengths. Note that in this study, we focus on light attenuation driven by CDOM absorption and disregard any backscattering effect from particulate matter. We acknowledge that the backscattering effect could play an important role in the SBS as the Mackenzie River is the Arctic's greatest exporter of particulate matter, but we aim here to build a foundation for determining the contribution of each component of terrestrial organic matter.

In our ED-SBS configuration, we approximated the relationship between CDOM light attenuation and its mass concentration (mmol C m⁻³) in high CDOM environments such as Arctic river-influenced waters. In this regard, we empirically estimated the CDOM diffuse attenuation coefficient (k_{CDOM} ; m⁻¹) from 31 in-situ measurements of the CDOM spectral absorption ($a_{CDOM}[\lambda]$; m⁻¹ nm⁻¹) across the SBS (Figure 2a.). The standard solar irradiance spectrum (ASTM G-173; U.S. D.O.E., 2005) was used as the reference shortwave solar spectrum at the surface ocean (Q_{sw_0} ; W m⁻² nm⁻¹) — terms are listed in

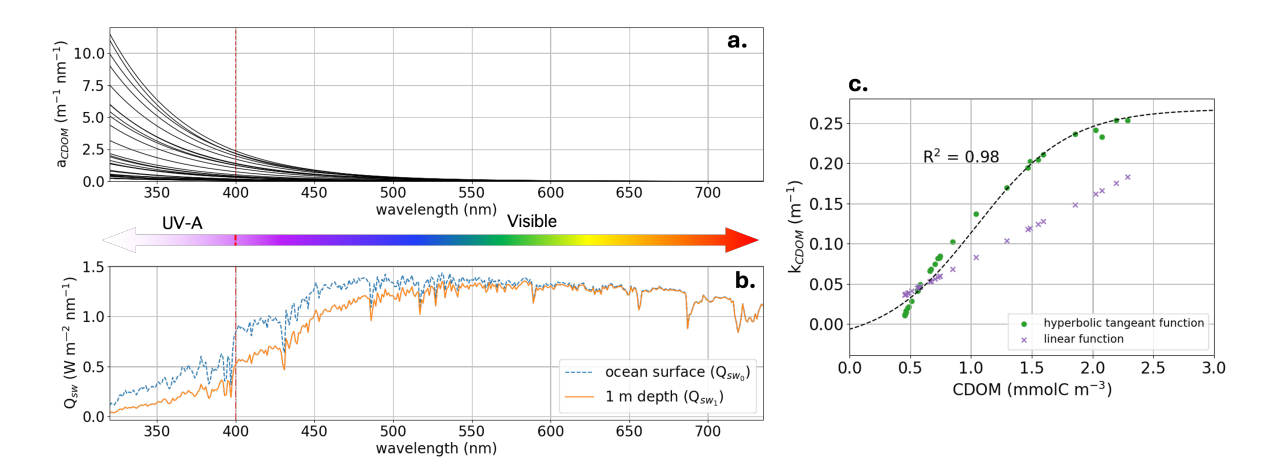


Figure 2. (a) In-situ CDOM spectral absorption measured over the Mackenzie Shelf during the 2009 Malina cruise for 31 water samples. (b) Shortwave solar spectrum (Q_{sw}) at the ocean surface (Q_{sw_0}) ; dashed blue line) and at 1-m depth after CDOM absorption (Q_{sw_1}) ; solid orange line). (c) CDOM attenuation (k_{CDOM}) relationship as it is described in Pefanis et al. (2020) (purple crosses) and in this study (green dots). The vertical red dashed line indicate the limit between UV-A and visible wavelength. Note that in Equation 1 we are computing the shortwave radiation absorbed from surface ocean to 1-m depth (Q_{sw_1}) , which results in the units being in W m⁻³ and hence k_{CDOM} having units of inverse meters.

Table A1. We first calculated the shortwave spectrum attenuated from the surface ocean to 1-m depth $(Q_{sw_1}; W m^{-3} nm^{-1})$ by multiplying Q_{sw_0} with $a_{CDOM}[\lambda]$ (Figure 2b.). Then, k_{CDOM} was retrieved by integrating Q_{sw_0} and Q_{sw_1} over the chosen wavelengths for each station using Equation 1.

$$140 \quad k_{CDOM} = 1 - \frac{\int_{\lambda} Q_{sw_1} d\lambda}{\int_{\lambda} Q_{sw_0} d\lambda},\tag{1}$$

where lambda is the discrete wavelength (nm). Then, CDOM concentrations were estimated from a_{CDOM} [440nm] (m⁻¹) using the relationship from Neumann et al. (2020) (Equation 2).

$$CDOM = \frac{a_{CDOM}[440nm] + 0.2409}{Mc \times 0.0478},$$
(2)

where Mc is the carbon atomic mass ($Mc = 12.0107 \text{ g mol}^{-1}$). Finally, we fitted a hyperbolic tangent function (Equation 3) to obtain the relationship linking k_{CDOM} and CDOM concentrations across the range of conditions found in the SBS (Figure 2c).

$$k_{CDOM} = a \times \tanh(b \times \text{CDOM} + c) + d. \tag{3}$$

As shortwave radiation and PAR were simulated independently in the physical and biogeochemical components of the model, we calculated two different sets of parameters for the k_{CDOM} /CDOM concentration relationship for both components. Both relationships yielded an R² of \geq 0.98. Parameters fitted with the full shortwave spectrum (used in the physical component) were: a = -0.15, b = -1.31, c = 1.04, and d = 0.12. Parameters fitted with PAR (used in the biogeochemical component) were: a = -0.14, b = -1.18, c = 1.04, and d = 0.10.

2.3 CDOM biophysical feedback

160

175

We included the effect of CDOM on light attenuation in the biogeochemical component of the model (which already included light attenuation by water and Chlorophyll-a (Chla)). PAR intensity (I(z), W m⁻²), at depth z is calculated according to the following equation:

165
$$I(z) = (1 - f_{ice}) \times 0.4 \times I_{sw} \times e^{-[k_w + k_{chla} \times chla(z) + k_{CDOM}(z)]dz},$$
 (4)

where I_{sw} (W m⁻²) is the shortwave downwelling irradiance (input from the physical component of the model), for which 40% is considered as PAR, f_{ice} is the ice-cover fraction, k_w is the diffuse attenuation coefficient for pure seawater ($k_w = 0.04 \text{ m}^{-1}$), k_{chla} is the Chla diffuse attenuation coefficient ($k_{chla} = 0.04 \text{ m}^2 \text{ mg Chla}^{-1}$), chla(z) (mg Chla m⁻³) is the total concentration in Chla at depth z, and k_{CDOM} is the diffuse attenuation coefficient for CDOM at depth z.

We included the biophysical feedback of CDOM light attenuation ocean warming by including k_{CDOM} , integrated over the entire shortwave spectra in the physical component of the model (see section 2.2). The physical component of the model already included the thermal effect of light attenuation by seawater, calculating a downwelling light decay profile (dk_{sw} ; 1-D) based on Jerlov water types (Paulson and Simpson, 1977) and decreasing from the ocean surface to seafloor starting with a value of 1 at the surface. We included the thermal effect of CDOM light attenuation by calculating a CDOM light decay profile (dk_{CDOM}) based on k_{CDOM} (equation 5), also decreasing with depth starting from from 1 at the surface. As CDOM concentrations are variable in space, the resulting light decay profile produces a 3-D field.

180
$$\begin{cases} dk_{CDOM}(0) = 1\\ dk_{CDOM}(z) = dk_{CDOM}(z-1) \times e^{-k_{CDOM}d(z-1)}, \end{cases}$$
 (5)

where $dk_{CDOM}(0)$, the decay at the surface ocean (0-m depth) is set to 1, since simulated light has not yet been affected CDOM and z-1 is the depth of the vertical grid cell above z. The dk_{CDOM} calculation is then propagated from the ocean surface to the seafloor, as its value at depth z depends on all the values above. We then multiplied both decay profile to yield the total decay profile (dk_{tot} ; 3-D) as follows:

$$dk_{tot}(z) = dk_{sw}(z) \times dk_{CDOM}(z). \tag{6}$$

The setup described above represents a significant advancement over the previous model development by Pefanis et al. (2020). We took the advantage of an extensive in-situ carbon dataset collected in 2009 to update the parameterization of CDOM mass fluxes as they transition between short and long-residence-time carbon loops, where it was previously represented using a single DOC pool (Dutkiewicz et al., 2015). We also revisited the k_{CDOM} /CDOM relationship, transitioning from a linear to a hyperbolic tangent relationship (see Figure 2c.) This is particularly relevant for river plume regions where CDOM concentration reaches high values. Finally, our developments included the heating contribution of CDOM UV-A absorption, which contributes to roughly 40% of CDOM light absorption in the Mackenzie shelf region. The ED-SBS setup presented here is thus able to better represent the terrestrial browning effect on Arctic coastal regions.

3 Results

185

195

200

205

The simulations presented herein include all model improvements detailed above (Run_{full}), *i.e.*, a CDOM tracer communicating with two DOC pools; CDOM light attenuation as a hyperbolic tangent function, including UV-A attenuation heating effect; and riverine input (see Table 1). For the remainder of the study, we focus our analysis on the year 2012 – different from parameterization year (2009) – for two reasons: 1) sea ice area showed a major reduction during this year (Parkinson and Comiso, 2013) and 2) previous results by Pefanis et al. (2020) focus on this specific year. However, all simulations were performed with the same forcings over 5 years (2008–2012) to mitigate spin-up effects in processes directly affected by the inclusion of CDOM, such as dissolved carbon (DOC and DIC) concentration, or indirectly affected such as nutrient stock through changes in primary productivity. We also limit our analysis to the Mackenzie River plume region, which we define by the time-mean sea-surface salinity (SSS) isohaline of 27 (Supporting Information Figure S1).

We also compute metrics that describe sea ice phenology, as defined in Bliss et al. (2019); these metrics are then spatially averaged over the plume region. The day of opening (DofO) and the day of closing (DofC) are respectively the first and last

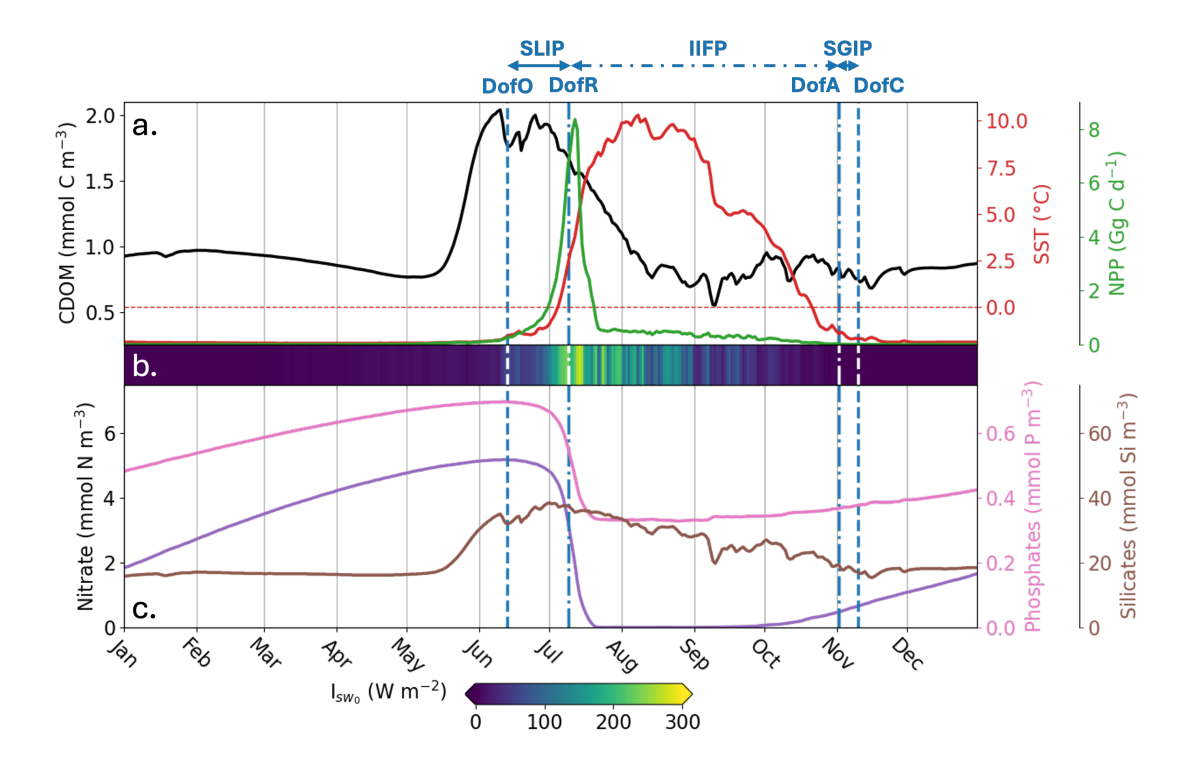


Figure 3. Spatially-averaged surface-ocean parameters simulated by $\operatorname{Run}_{full}$ in the Mackenzie River plume during 2012. Parameters shown are: (a) CDOM concentration (mmol C m^{-3} ; black line), SST (°C; red line), NPP (Gg C d^{-1} ; green line), (b) shortwave downwelling irradiance at the ocean surface ($\operatorname{I}_s w0$; W m^{-2}), (c) nitrate concentration (mmol N m^{-3} ; purple line), phosphate concentration (mmol P m^{-3} ; pink line) and, silicate concentration (mmol Si m^{-3} ; brown line). The vertical dotted blue lines show the spatial-mean day of opening (DofO) and day of closing (DofC) and the vertical dashed-dotted blue lines show the spatial-mean day of retreat (DofR) and day of advance (DofA). Sea ice melting periods are shown consecutively, the seasonal loss of ice period (SLIP), the inner ice-free period (IIFP), and the seasonal gain of ice period (SGIP).

days when sea ice concentration is below 80%. The day of retreat (DofR) and the day of advance (DofA) are respectively the
first and last days when sea ice concentration is below 15%. The period between these two days is the inner ice-free period
(IIFP) or open-water period. The period between DofO and DofR is defined as the seasonal loss of ice period (SLIP) and the
period between DofA and DofC is the seasonal gain of ice period (SGIP). The above metrics are summarized in a schematic
(see Appendix C) and are also indicated on the top of the following figures.

5 3.1 Mackenzie River plume seasonal phenology

We first describe the seasonal phenology of several important physical and biogeochemical variables in the simulated Mackenzie River plume. In the river plume, Run_{full} simulates an average surface CDOM concentration of 0.85 ± 0.08 mmol C m⁻³

Table 1. Characteristics of the simulations tested in this study.

Experiment name	\mathbf{k}_{CDOM}	CDOM heating	CDOM river input
Run_{full}	hyperbolic tangent	UV-A & visible	yes
$\operatorname{Run}_{noriv}$	hyperbolic tangent	UV-A & visible	no
Run_{lin}	linear	visible (PAR)	yes
$\operatorname{Run}_{ctrl}$	off	off	yes
Run_{light}	hyperbolic tangent	off	yes

Changes to Run full are highlighted in bold.

from August to May, with a peak of 2.04 mmol C m⁻³ during the spring freshet, followed by declining concentrations in July (Figure 3, black line). With regard to the sea ice phenology in the river plume, the model simulates an open-water period of \sim 4 months (115 days), with SLIP and SGIP lasting 1 month (June 13 to July 9) and 1 week (November 2 to 10), respectively. From January to June, the SST is on average near the seawater freezing temperature (-1.93°C) and slowly starts heating up in June with increasing shortwave downwelling irradiance at the ocean surface (I_{sw_0} ; Figure 3b.) and accelerating freshwater discharge. In July, ocean-surface shortwave downwelling irradiance reaches a maximum, rapidly heating SST until it reaches a peak value of 10.3°C on August 8. Then, temperatures slowly cool until the end of SGIP. Phytoplankton rapidly bloom during the SLIP period, with a peak in surface NPP of 8.35 Gg C d⁻¹ occurring two days after DofR. The production period — defined as the duration when NPP exceeds half of its maximum — lasts 7 days (July 7 to 14) and coincides with the period when subsurface light is the most intense. Nitrate and phosphate are quickly consumed during the phytoplankton bloom until the nitrate stock is depleted. Nutrient stocks are replenished through vertical mixing, advective transport, and remineralization from October to June. The simulated silicate tracer is directly connected to DSi riverine mass flux and therefore increases with elevated runoff.

Within the Mackenzie River plume region, Run_{full} captures the mean SST amplitude and variability during the open-water period depicted by observations (Figure D1). The model underestimates SST by 17% from mid-July to mid-September. This is due to a later simulated SLIP, which delays surface-ocean heating and causes simulated SST to increase later in the season. Run_{full} also reasonably reproduces the amplitude of the phytoplankton bloom observed by remote sensing, as the simulated surface-ocean Chla peaks at approximately the same concentration as reported by Lewis et al. (2020). However, the model underestimates the bloom's duration, simulating a bloom that lasts only half as long as observed by satellite. This discrepancy arises from the model's later simulated SLIP (similar to its SST behavior) and the rapid depletion of nitrates during the late open-water period. A more detailed and comprehensive model-data evaluation for 2012 is provided in Appendix D.

220

225

230

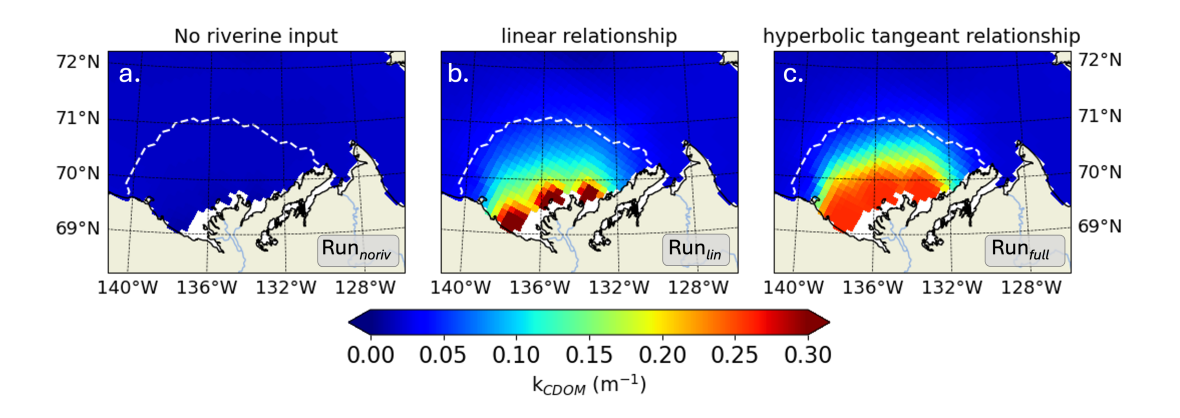


Figure 4. For July 2012, time-mean CDOM diffuse attenuation coefficient (k_{CDOM} , m⁻¹) for (a) Run_{noriv}, (b) Run_{lin}, and (c) Run_{full}. The white dashed line marks the time-mean spatial extent of the Mackenzie River plume.

3.2 Adding riverine CDOM to ED-SBS

We next explore how the inclusion of riverine CDOM impacts light attenuation characteristics on the Mackenzie River shelf by comparing $\operatorname{Run}_{full}$ (presented above) to two similar set-ups: 1) excluding CDOM riverine forcing ($\operatorname{Run}_{noriv}$; autochthonous CDOM only) and 2) using a linear CDOM light attenuation only in visible light (similar to Pefanis et al. (2020); Run_{lin}). We analyze the differences for the month of July, when shortwave downwelling irradiance (I_{sw}) is maximum and terrestrial CDOM is more likely to affect the biophysical characteristics of the plume region. The simulation excluding river mass flux exhibits a space-time mean k_{CDOM} of $0.02~\mathrm{m}^{-1}$ ($\operatorname{Run}_{noriv}$) in the plume region (Figure 4a). Including riverine CDOM increases k_{CDOM} to $0.13~\mathrm{m}^{-1}$ and $0.16\mathrm{m}^{-1}$ when using a linear (Run_{lin}) and hyperbolic tangent ($\operatorname{Run}_{full}$) relationship with CDOM, respectively. In the vicinity of the river mouth, k_{CDOM} reaches values 6.5 to 8 times higher than simulations without riverine CDOM forcing, highlighting the importance including the riverine CDOM effect on light in the nearshore region. When using a linear relationship, k_{CDOM} increases as CDOM concentration increases, triggering high values (>0.3 m⁻¹ with a maximum at 0.59 m⁻¹) in the direct vicinity of the river mouth, with a sharp transition to lower values further offshore (<0.2 m⁻¹) (Figure 4b.). When using the hyperbolic tangent relationship, k_{CDOM} is capped to 0.26 m⁻¹, given the $\operatorname{k}_{CDOM}/CDOM$ relationship fitted with in-situ observations (see Figure 2c.). As a result, CDOM attenuation is more evenly spread along the nearshore region (Figure 4c.).

3.3 Riverine CDOM biophysical feedback

250

255

We now examine how riverine CDOM influenced the physical conditions of the SBS during 2012, introducing a control simulation (Run_{ctrl}) that differs from Run_{full} by turning off both CDOM light attenuation (Section 2.2) and its effect on seawater

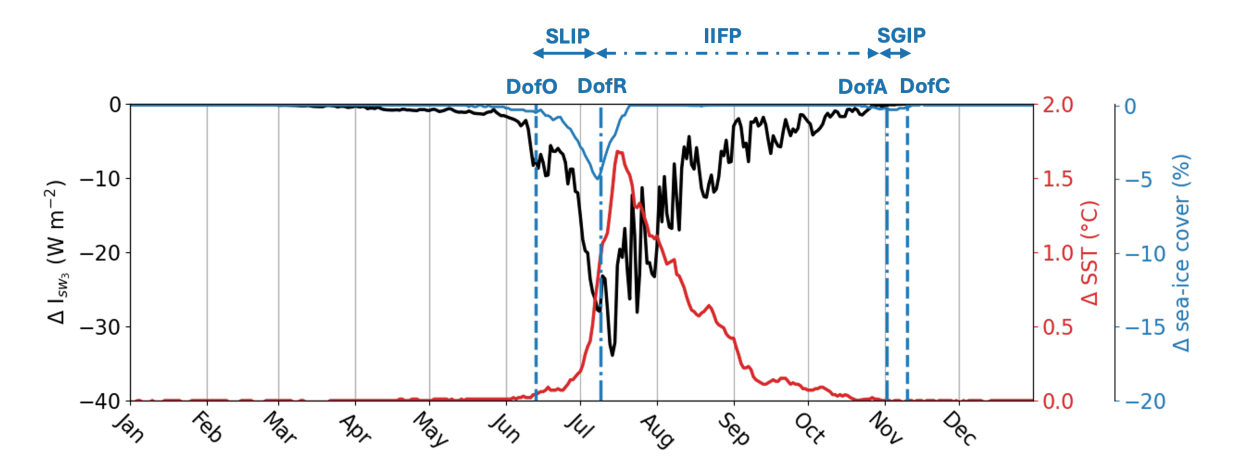


Figure 5. Difference in subsurface shortwave downwelling irradiance at 3m depth (I_{sw_3} in W m^{-2} ; black line), SST (°C; red line) and sea ice concentration (%; blue line) between Run_{full} and Run_{ctrl} . The vertical dotted blue lines show the spatial-mean Day of Opening (DofO) and Day of Closing (DofC) and the vertical dashed-dotted blue lines show the spatial-mean Day of Retreat (DofR) and Day of Advance (DofA) simulated by Run_{full} .

heating (section 2.3) (see Table 1).

260

265

270

In the river plume, $\operatorname{Run}_{full}$ simulates a peak of surface CDOM concentration during the spring freshet, which coincides with the SLIP and the increase in surface-ocean shortwave downwelling irradiance (Figure 3). As a result, the subsurface shortwave irradiance (I_{sw_3}) — defined as the shortwave irradiance ($\operatorname{W} m^{-2}$) below the model surface layer (3-m depth) — decreases by 13.4 W m^{-2} (40%) on average during the SLIP (Figure 5) compared to the simulation without CDOM effects ($\operatorname{Run}_{ctrl}$). CDOM light attenuation in the plume region then triggers an additional SST increase ($\operatorname{\Delta SST}$ up to 1°C), driving a decrease in sea ice cover by up to 5% (Figure 5). We note a delay of 1 day in the DofR in $\operatorname{Run}_{full}$ compared to $\operatorname{Run}_{ctrl}$ (not shown), demonstrating the limited influence of riverine CDOM on sea ice phenology. Terrestrial CDOM has a maximum impact on the physical condition of the plume one week after the DofR, with a 45% decrease in subsurface shortwave downwelling irradiance and an increase of by up to 1.68°C (Figure 5). Finally, the impact of riverine CDOM gradually diminishes as the tracer becomes diluted in the open ocean during the IIFP.

Following the approach in subsection 3.2, we analyze the influence of the k_{CDOM} parameterization on the river plume's temperature by comparing the changes in SST simulated by Run_{noriv} , Run_{lin} , and Run_{full} , relative to Run_{ctrl} . We focus on the month of July, when CDOM has the greatest impact on SST in the Mackenzie River plume (Figure 6). In Run_{noriv} , the change in CDOM heating relative to Run_{ctrl} is solely attributed to marine CDOM produced by phytoplankton grazing and mortality. The spatially-averaged change in SST due to phytoplankton-generated CDOM, based on the improved CDOM-carbon loop connection (see section 2.1), is $0.45 \pm 0.09^{\circ}C$. The specific contribution of riverine CDOM leads to increases of 84% (0.83)

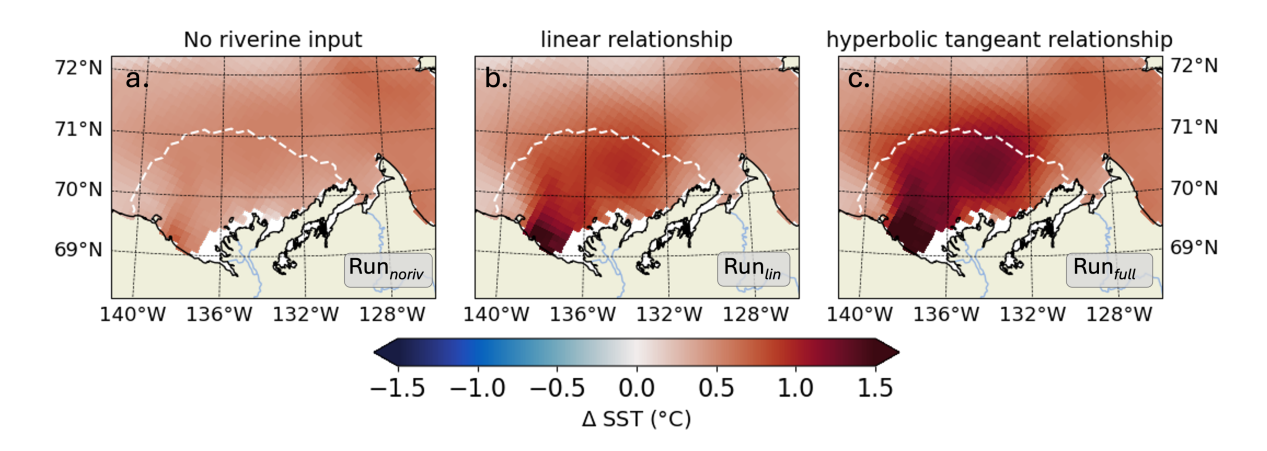


Figure 6. Time-mean SST differences (°C) for July 2012 between (a) Run_{noriv} , (b) Run_{lin} , and (c) Run_{full} , relative to the baseline simulation which excludes the CDOM effect (Run_{ctrl}). The white line in each panel indicates the mean extent of the Mackenzie River plume.

± 0.24°C, Run_{lin}) and 144% (1.10 ± 0.28°C, Run_{full}) using the linear and hyperbolic tangent k_{CDOM}/CDOM relationships, respectively. We note that the k_{CDOM} relationship in Run_{lin} only considers a classic linear CDOM warming effect resulting from PAR attenuation, emphasizing the dominant role of UV-A in SST warming.

3.4 CDOM effect on marine primary productivity

285

290

295

In the remainder of the study, we explore the specific effects of CDOM light attenuation and ocean heating on the coastal primary producers and the carbon cycle, focusing on the biological and solubility pump. From here, we only focus on three simulations: Run_{full} , Run_{light} , and Run_{ctrl} . The later two simulations deviate from Run_{full} by turning off aspects of the CDOM light absorption (see Table 1): $In Run_{ctrl}$, we turn off both CDOM light attenuation (Section 2.2) and its effect on seawater heating (section 2.3). $In Run_{light}$, we turn off only the CDOM heating effect (section 2.3) but include its effect on light attenuation. We then disentangle the individual impacts of light attenuation and their influence on ocean temperature over seasonal timescales.

Annual surface-ocean NPP integrated in the river plume region remains similar across simulations, whether including the influence of CDOM on light and temperature (Run_{full}) or not (Run_{ctrl}), yielding 0.10 and 0.13 Tg C yr⁻¹, respectively. However, a mean delay of 15 ± 3 (min: 9-max: 23) days occurs in the seasonal phytoplankton bloom, defined here as the day when Chla reaches its peak value. The surface-ocean NPP maximum, initially occurring in the middle of SLIP, is delayed to DofR by the end of the sea ice melt season due to CDOM (Figure 7a). Introducing both CDOM light and biophysical parameterizations (Run_{full}) results in a 85% increase in peak NPP, with 78% attributed to the change in CDOM/light interactions and 7% to increasing SST. However, the production period — defined as the duration when NPP exceeds half of its maximum — decreases

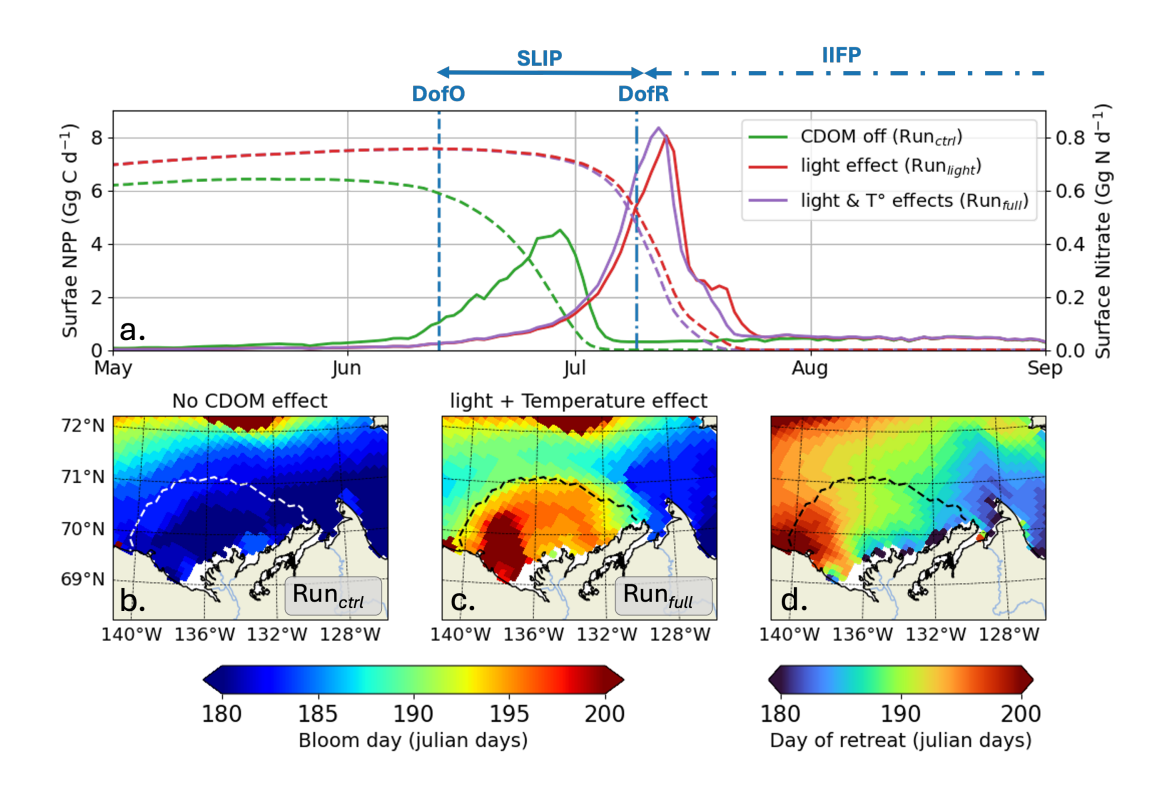


Figure 7. (a) Surface-ocean NPP (Gg G d⁻¹; thick lines) and nitrate stock (Gg N d⁻¹; dashed lines) simulated by ED-SBS without the CDOM light attenuation effect (green line; Run_{ctrl}), including 1) CDOM PAR light attenuation (red line; Run_{light}) and 2) CDOM light attenuation and ocean warming effect (purple line; Run_{full}). Maps of bloom day (julian days) (b) without the CDOM light attenuation effect, (c) including CDOM PAR light attenuation, and (d) map of DofR (julian days) simulated by EDS-SBS. Dotted line on the maps show the time-mean SSS isohaline of 27; vertical dotted and dashed-dotted blue lines show the DofO and DofA, respectively.

from 12 to 5 days, thereby explaining the similar annual NPP.

300

305

310

By early June, surface-ocean nutrient stocks are replenished through vertical mixing, advective transport, and remineralization that primarily occurred during winter – Note that the differences in May surface nitrate concentrations observed in Figure 7a are related to changes in stock replenishment over the spin up period due to CDOM inclusion. High sea ice concentrations during most of the year result in light availability being primary limiting factor for phytoplankton growth, with temperature as a background limitation (See Appendix E). As the season progresses into SLIP the sea ice concentration decreases, leading to higher light penetration into upper-ocean waters. In Run_{ctrl} , this allows phytoplankton to utilize nutrients and initiates a bloom (Supporting Information Figure S2a.) that persists until the nitrate stock is entirely consumed and thus limits further phytoplankton growth. However, by early June, riverine CDOM (Run_{light}) drives additional light attenuation, counterbalancing the increased light penetration resulting from sea ice loss (see Figure 5), hence slowing down the bloom initiation and delaying it by roughly 2 weeks (see Figure 7 and Supporting Information Figure S2b). Consequently, phytoplankton bloom latter in

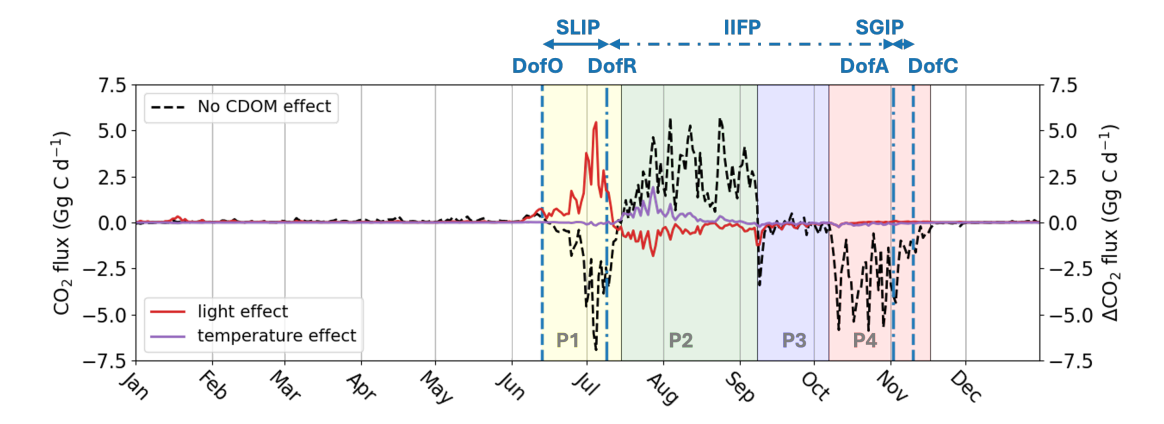


Figure 8. Air-sea CO_2 flux $(Gg \ C \ d^{-1})$ simulated by Run_{ctrl} in the plume region without CDOM biophysical feedback effects (black dotted line) and the change in air-sea CO_2 flux $(Gg \ C \ d^{-1})$ induced by the PAR light attenuation effect (red thick line) and warming effect (purple thick line). The vertical dotted blue lines show the average DofO and DofC and the vertical dashed-dotted blue lines show the average DofR and DofA. Phases with a switch in air-sea CO_2 flux simulated by Run_{ctrl} are indicated by four colors (P1: yellow, P2: green, P3: blue, and P4: red)

the season until the nitrate stock is exhausted and again limits further growth. We find an east-west gradient in the maximum bloom day (Figure 7c), correlated with the DofR (Figure 7d). This supports our hypothesis that light attenuation from riverine CDOM export complements light attenuation from sea ice during the melting period and delays the seasonal phytoplankton bloom until the open-water period.

315 3.5 CDOM effect on coastal air-sea CO2 fluxes

320

325

In the absence of CDOM effects (light and heating effect), Run_{ctrl} results in a net annual CO_2 sink of -11.40 Gg C yr⁻¹ within the plume region. Over seasonal timescales, air-sea CO_2 exchange occurs from DofO to DofC, with four distinct phases (Figure 8). The following figures show the net air-sea CO_2 flux, integrated within the river plume region over the time period considered. The initial phase, starting from DofO and extending to one week after DofR, exhibits a substantial net CO_2 sink of -53.2 Gg C, which is attributed to phytoplankton growth (see Figure 7). Following this, the second phase, which spans two months at the onset of the inner ice-free period (IIFP), is marked by a significant net CO_2 outgassing of 137.9 Gg C — this results from the decline in phytoplankton abundance and heightened local concentrations of DIC/DOC from river discharge (Bertin et al., 2023). Subsequently, a less-variable, one-month long phase follows, characterized by a delicate balance (air-sea CO_2 flux near $0 \text{ Gg C } d^{-1}$) that results in a moderate net uptake of -10.3 Gg C. The third phase, starting in early October and extending to one week after DofC, exhibits a strong net CO_2 sink of -99.2 Gg C. During this last phase, phytoplankton declines due to depleted nitrate levels and DIC/DOC concentrations return to background levels as river discharge diminishes.

Over seasonal timescales, substantial changes in the timing and patterns of air-sea CO_2 flux occur during the two initial phases due to the inclusion of CDOM effects. As a result of CDOM light attenuation, we observe a delay in phytoplankton activity from the first phase (prior to DofR) to the subsequent phase (Figure 7), leading to a 79% reduction in simulated CO_2 uptake during phase 1 (+42.0 Gg C; Figure 8). Furthermore, the increase in SST due to CDOM is minimal during this period (Figure 5), resulting in an negligible impact on net air-sea CO_2 flux (0.4 Gg C).

As the phytoplankton bloom simulated by Run_{full} peaks at the onset of the second phase, CDOM light attenuation reduces net CO₂ outgassing by 47.0 Gg C. However, the warming effect of SST counteracts the reduced CO₂ outgassing (caused by phytoplankton growth), driving a CO₂ outgassing of 19.8 Gg C during this period. Consequently, the net CO₂ outgassing for this period is reduced by 27.2 Gg C. Comparing the loss in CO₂ uptake on the first period (42.0 Gg C) and the gain in CO₂ uptake (-27.2 Gg C), the reduction in the CO₂ sink during the first period is 14.8 Gg C higher than the gain in the second period. Thus, changes in CO₂ fluxes during these two periods represent 80% of the annual net loss in CO₂ sink. As a consequence, when including the CDOM bio-physical feedback (Run_{full}), the plume switches to a net annual CO₂ outgassing of 7.35 Gg C yr⁻¹. We show here that, despite the greater effect of light attenuation on the magnitude and sign of air-sea CO₂ flux, the temperature effect is the dominant contributor in the transition of the plume from a sink to a source of CO₂, as it dampens the increased CO₂ uptake due to phytoplankton growth in early summer.

4 Discussion

355

330

Assessing air-sea CO₂ fluxes in Arctic coastal environments remains challenging, as the carbon cycle and ecosystems are affected by a wide range of physical and biogeochemical processes that span the land-ocean continuum. As 11% of the global river discharge is fluxed into the Arctic Ocean (McClelland et al., 2012), coastal waters are highly influenced by terrestrial browning (Lewis et al., 2020; Li et al., 2024), motivating the need to include this effect in ocean biogeochemistry models. In this study, we develop a new regional-scale ECCO-Darwin model that simulates 1) the impact of marine CDOM on the physical properties of the water column (Kim et al., 2018; Gnanadesikan et al., 2019; Pefanis et al., 2020) and 2) the interaction of terrestrial CDOM with the marine carbon cycle (Neumann et al., 2021; Clark et al., 2022).

Our model includes CDOM light attenuation (k_{CDOM}) as a hyperbolic tangent function of CDOM concentration, estimated from in-situ observations of CDOM spectral absorption from 280–750 nm on the Mackenzie Shelf. Using this relationship, simulated CDOM in the plume region compares reasonably well with both in-situ and satellite measurements (Matsuoka et al., 2012, 2017; Massicotte et al., 2021, see Appendix B). Furthermore, we show that using a hyperbolic tangent for k_{CDOM} limits the effect of CDOM light attenuation in high CDOM concentration regions, allowing for the light attenuation from CDOM to be distributed more evenly along the nearshore region (Figure 4). Based on these results, we suggest that similar relationships be used in future models that aim to realistically represent coastal regions where CDOM concentrations reach high values (CDOM>1.3 mmol C m⁻³ i.e., a_{CDOM} (440)>0.5 m⁻¹; Matsuoka et al., 2012). Additionally, this relationship was calculated

from CDOM absorption integrated over the entire shortwave spectra, which includes the UV light absorption component, which is estimated to contribute up to 40% of CDOM absorption on the Mackenzie Shelf. Therefore, our study considers the complete effect of CDOM attenuation on ocean heating, inducing a 36% increase in the seasonal cycle of SST compared to previous methods (CDOM heating from PAR and k_{CDOM} as a linear relationship; see Run_{lin} and Gnanadesikan et al., 2019; Pefanis et al., 2020; Neumann et al., 2021).

Many ocean biogeochemistry models now incorporate land-to-ocean nutrient fluxes (Terhaar et al., 2019; Lacroix et al., 2021; Savelli et al., 2025), however, ocean circulation and physics often drive the biogeochemical state without the potential feedback of biogeochemistry on physics. In Arctic coastal regions, CDOM absorption has been reported to be a significant factor in the ocean heat budget (Hill, 2008; Soppa et al., 2019), but models still fail to include this feature. We find that including the CDOM heating effect in ED-SBS improved the model's ability to simulate the space-averaged SST observed during the early open-water season (Good et al., 2020, See Appendix D). We further show that riverine CDOM absorption contributes to a 1.7°C increase in SST in the Mackenzie River plume, which is consistent with the increased seasonal amplitude previously reported for the AO (Gnanadesikan et al., 2019). The maximum increase occurs at the onset of the open-water season (0.2°C/day), which is the same order of magnitude as observed in the Laptev Sea (Soppa et al., 2019). Although our model includes a component of CDOM generated by phytoplankton mortality and its associated light attenuation, we lack light attenuation by Chla (Dutkiewicz et al., 2019), which has been shown to increase the SST signal by ~0.5°C along the Arctic continental shelves (Lengaigne et al., 2009). We note that the simulated increase in SST has a limited impact on sea ice, as we observe only a 5% decrease in sea ice cover and a change in DOR by a single day.

By adding CDOM light attenuation to ED-SBS, we also observe a change in the simulated Mackenzie River plume phytoplankton bloom phenology. During the freshet season (early June), in Run_{full} , riverine CDOM triggers a small difference in light limitation (see Appendix E), which delays the phytoplankton bloom by two weeks to the end of melting season. As a result of increased light penetrating the water column, the simulated phytoplankton bloom amplitude is 85% higher and 1 week shorter due to rapid nitrate consumption. In the plume region, we further observe a westward gradient in the phytoplankton bloom peak day, which is correlated with the day of sea ice retreat (Figure 7 c. and d.). These results highlight that the coupling between CDOM and sea ice play a dominant role in shaping phytoplankton phenology, while the CDOM heating effect has a second order effect.

Further comparing simulated Chla and primary productivity with satellite observations (Lewis et al., 2020) in the Mackenzie River plume (Note that this time-series are calculated where observations are available; more details in Appendix D), Run_{ctrl} and Run_{full} overestimate the average maximum in surface Chla by 55% and 62%, respectively (Figure 9a). However, Run_{full} better simulates the spatial distribution of surface Chla especially in the vicinity of the coast (see Figure D1). Run_{full} also successfully simulates the maximum in NPP observed by satellite (28 Gg C d⁻¹) while Run_{ctrl} underestimate it by 13%. However, with respect to the initiation of the bloom Run_{ctrl} better matches observations (surface Chla and NPP), where Run_{full}

bloom initiate with 2 to 3 weeks delay. Looking into more details on the sea ice melting behavior (SLIP equivalent with or without CDOM), we find that ED-SBS exhibits a shorter 2012 SLIP, with a 24-days delay in the DofO and a 16-day delay in the DofR. We therefore acknowledge that the combination of sea ice and CDOM light attenuation (Run_{full}) triggers the correct phenology in phytoplankton bloom initiation with respect to sea ice melting, but the incorrect timing as the bloom initiates 3 weeks later due to delayed DofO. This behavior in relation to the sea ice is confirmed in the comparison of averaged SST in the Mackenzie River plume (more details in Appendix D). As observed melting season starts mid-May, SST rises in early June when DofR approaches, while simulated melting season only kicks in mid-June – 1 month after the observations – allowing a rise in SST by the beginning of July. Finally, the observed production remains high latter in the open-water season (August to September); ED-SBS is not able to sustain a high rate of primary productivity during this period as nitrate is entirely consumed, shutting down the bloom. The low simulated levels of Chla after the bloom could be attributed to a match-mismatch with zooplankton.

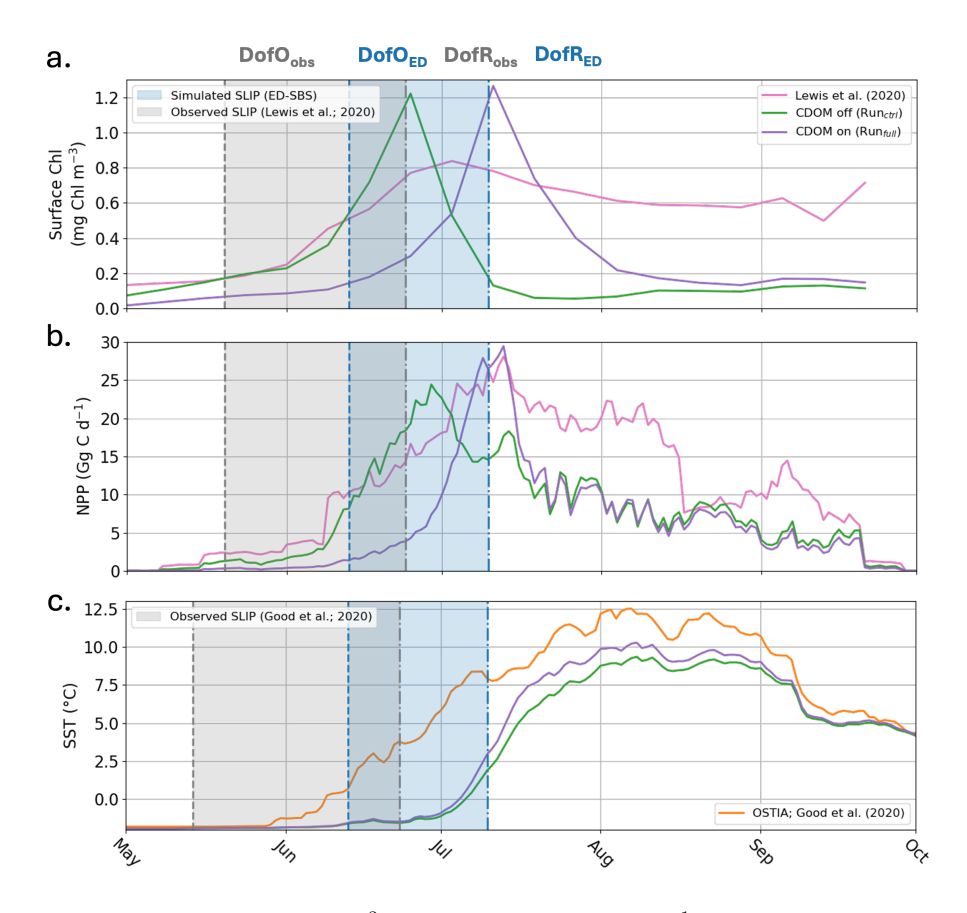


Figure 9. 2012 (a) averaged Surface Chla (mg Chla m^{-3}), (b) integrated NPP (Gg C d^{-1}), and (c) averaged SST ($^{\circ}$ C) over the Mackenzie River plume region for Run_{ctrl} (green line), Run_{full} (purple line), satellite observations (pink line Lewis et al., 2020), and in-situ/satellite observations (orange line Good et al., 2020). The blue (grey) area indicates the simulated (observed) seasonal loss of ice period.

We argue that including CDOM does not necessarily improve the phytoplankton phenology in the Mackenzie River plume compared to observations but does enhance its behavior regarding to sea ice melting. Furthermore, biophysical feedback of CDOM on water heating plays a non-negligible role in simulating SST in the region. We note that further improvements to the sea ice model and its interaction with phytoplankton would be required to accurately simulate the initiation of the bloom. The next version of ED-SBS, which will have high horizontal (~ 1 km) and vertical resolution (~ 1 m at the surface), will permit improved representation of fine-scale sea ice dynamics, such as cracks, leads, and specific features of the Mackenzie Delta such as the Stamukhi (Carmack and Macdonald, 2002; Matsuoka et al., 2016). Including melt ponds in future version of the model will also be necessary to improve the initiation of the phytoplankton bloom, as their impact on light penetration through sea ice has been reported to be important for the development of under-ice blooms (Ardyna and Arrigo, 2020; Clement Kinney et al., 2023). This might have an important effect as early snow melt and sea ice breakup as shown to enhance algal export in the Beaufort Sea (Nadaï et al., 2021). Finally, as a consequence of climate change and delayed sea ice freeze-up, Arctic phytoplankton phenology has been reported to transition to double bloom characteristics (Manizza et al., 2023); with a spring bloom initiated by under-ice blooms and low-light-adapted diatoms followed by an autumn bloom characterized by low-nitrogen adapted phytoplankton (Ardyna and Arrigo, 2020). The inclusion of the latter ecosystem components in ED-SBS could improve the phytoplankton representation in the latter open-water period, as our ecosystem is rapidly limited by nitrate concentrations. Furthermore, this hypothesis aligns with previous work by Choi et al. (2024), who showed that the inclusion of a nitrogen fixer (not dependent on nitrate) could explain the secondary fall bloom.

425

430

435

420

410

While the CDOM heating effect has a limited impact on phytoplankton phenology, its role in modulating air-sea CO_2 fluxes is crucial, especially for the annual budget. With the inclusion of CDOM light attenuation, and as a consequence of two weeks delay of the phytoplankton bloom, the strong CO_2 uptake that occurs during the melting period (without CDOM effect) disappears and shifts into a dampening of the early open-water period CO_2 outgassing (Figure 8). Over annual timescales, this results in a decrease in the net CO_2 sink of 4.6 Gg C yr⁻¹, with the Mackenzie River plume region remaining a CO_2 sink. However, the inclusion of the CDOM heating effect and the $1.7^{\circ}C$ increase in SST at the onset of the open-water season promotes an increase in CO_2 outgassing due to reduced p CO_2 solubility, which balances the decrease in CO_2 outgassing driven by the phytoplankton bloom. Annually, CDOM heating promotes a 14.1 Gg C yr⁻¹ decrease in CO_2 uptake and switches the Mackenzie River plume region to a net CO_2 outgassing of 7.35 Gg C yr⁻¹. Although the contribution of Mackenzie River to the Arctic CO_2 budget is small (Yasunaka et al., 2023), we demonstrate that CDOM is an important factor contributing to CO_2 fluxes in coastal regions. In the future, the projected increase in terrestrial organic matter fluxes may drive elevated CDOM levels in Arctic coastal regions, thus affecting the solubility pump and local marine ecosystems (Nguyen et al., 2022). This effect is likely to be even more important in the Eurasian Basin, where terrestrial CDOM export is more pronounced (Stedmon et al., 2011).

440

Our study focuses on the Mackenzie River plume region, which is the main contributor of particulate organic carbon (POC) at the pan-Arctic scale (McClelland et al., 2016). Similarly to CDOM, terrestrial POC fluxes are likely to increase in the future

with increased runoff, permafrost thaw, and coastal erosion (Doxaran et al., 2015; Nielsen et al., 2024; Sauerland et al., 2025). The additional amount of carbon exported to the coastal water by erosion alone could decrease the Arctic Ocean CO₂ uptake by 7–14% by 2100 (Nielsen et al., 2024). Particulate organic matter also decreases the light available for primary production through absorption and backscattering (Stramski et al., 2004; Wozniak and Dera, 2007), potentially having an even stronger effect on the phenology. The effect of particle light backscattering may however overtake the effect of absorption, likely driving a decrease in coastal CO₂ uptake mainly by lower phytoplankton production rather than increased heat as shown with CDOM in this study. We acknowledge that ED-SBS does not account for terrestrial POC mass flux and the effect of suspended particulate matter on the attenuation of light (backscattering effect), which might be significant in this region (Lizotte et al., 2023). However, we focus here on the effect of the dissolved fraction and do not explore further assumptions regarding the particulate fraction effect, since our model does not account for solid sedimentation parameterization and bottom-sediment/seawater interactions. Future work will focus on the addition of a sediment model to fill this gap (Sulpis et al., 2022). Combined with the new Plankton, Aerosol, Cloud, ocean Ecosystem (PACE) satellite mission, which includes a hyperspectral imaging radiometer, the next generation of ED-SBS will be able to disentangle signature of Chla, CDOM, and particulate matter to better estimate coastal Arctic CO₂ fluxes. Finally, the ECCO framework has paved the way for adjoint modeling at the global-ocean scale (Brix et al., 2015; Carroll et al., 2022). Future simulations will use adjoint modeling to optimize ED-SBS based on available physical and biogeochemical observations in the SBS.

460 5 Conclusions

445

450

455

465

470

We developed a new regional AO model which includes terrestrial CDOM export from the Mackenzie River. The CDOM component interacts with the marine dissolved carbon pool and its feedback on the physical properties of the water column, such as light intensity and temperature. In particular, ED-SBS simulates spectrally-resolved UV-light absorption, which has been thus far ignored in model studies and is estimated to contribute to 40% of the light absorption in the SBS. We also suggest a new CDOM attenuation relationship as a hyperbolic tangent of CDOM concentration, which is able to better simulate light absorption in high CDOM concentration environments, such as river plumes.

In the plume region, we find that neglecting the coupled effects of light attenuation from sea ice cover and riverine CDOM export accelerates the timing of the simulated seasonal phytoplankton bloom by 2 weeks. Including riverine CDOM influence, the bloom occurs after the melting season, where light conditions are optimal, with a simulated phytoplankton bloom 85% higher than simulations without effect of CDOM, but also 1 week shorter due to quicker consumption of nitrate. We further find that including the riverine CDOM biophysical feedback switches the net CO₂ sink in the plume region from -11.40 Gg C yr⁻¹ (without CDOM effects) to a net outgassing of 7.35 Gg C yr⁻¹. Although the change in phytoplankton phenology has limited impact on the air-sea CO₂ fluxes, we find that the simulated outgassing is driven by reduction in pCO₂ solubility resulting from a 1.7°C increase in SST. Our modeling study demonstrates the importance of CDOM biophysical feedback in

Arctic river plume regions, and the strong implications of CDOM radiative heating on pCO₂ solubility and air-sea CO_2 fluxes. Our results suggest that future climate change induced increases in terrestrial organic matter exports could substantially affect ecosystems and air-sea CO_2 fluxes in shallow Arctic coastal regions where CDOM export is high.

Appendix A: List of terms

Table A1. List of terms used in this study

Terms	Abbreviation	Unit	Definition
Shortwave solar spectrum	Q_{sw}	$\mathrm{W}~\mathrm{m}^{-2}~\mathrm{nm}^{-1}$	Solar irradiance spectrum – at the surface of the ocean
			it corresponds to ASTM G-173 standard spectrum
Shortwave downwelling irradiance	I_{sw}	${\rm W}~{\rm m}^{-2}$	Integrated solar irradiance used in the physical
			component of the model
CDOM diffuse attenuation coefficient	k_{CDOM}	m^{-1}	loss of light intensity through CDOM.
CDOM absorption	a_{CDOM}	$\mathrm{m}^{-1}~\mathrm{nm}^{-1}$	loss of light absorbed by CDOM for each wavelength

480 Appendix B: Terrestrial CDOM ratio validation

500

505

We set the percentage of DOC_{sr} redistributed into the CDOM pool by performing a sensitivity experiment. Three different parameterizations of the riverine CDOM input were tested: Marine CDOM tracer is forced at the Mackenzie River mouth by a. 1%, b. 2%, and c. 4% of the total riverine tDOC mass flux. This percentage is subtracted from DOC_{sr} to CDOM as detailed in section 2.1 (Figure 1). Then, we compared the simulated light CDOM absorption $(a_{CDOM}[\lambda])$ derived from simulated CDOM concentration (see equation B1; Dutkiewicz et al., 2015) in the Mackenzie river plume, with in-situ observations of $a_{CDOM}[440\text{nm}]$ measured during the Malina Campaign (see location of station in Figure S1; Matsuoka et al., 2012; Massicotte et al., 2021) and remotely-sensed $a_{CDOM}[443\text{nm}]$ (Matsuoka et al., 2017).

$$a_{CDOM}[\lambda] = C_{CDOM} \times e^{-S_{CDOM}(\lambda - \lambda_0)} \times CDOM, \tag{B1}$$

where λ_0 is the reference waveband ($\lambda_0 = 450$ nm), C_{CDOM} is the CDOM absorption at λ_0 ($C_{CDOM} = 0.18$ m² mmolC⁻¹), and S_{CDOM} is the CDOM absorption spectral slope ($S_{CDOM} = 0.018$ m⁻¹).

We used 4 comparison metrics to compare retrieved CDOM absorption ($a_{CDOM}[\lambda]$) from simulated CDOM against observations: the median (\pm standard deviation), the correlation coefficient (r), the median percent error (MPE) and the unbiased root-mean-square error (MPE). Additional information and equations for the comparison metrics are detailed in Supporting Information Text S3. We find that changing the percentage of tDOC forcing CDOM as no impact on the correlation coefficient (Table B1). Size of discrepancies between the simulated and observed values (URMSE) are equivalent when riverine CDOM takes 1% or 2% of tDOC input but increases by 55 to 117% when forcing is set to 4%. The MPE increases by 40% to 89% when doubling the tDOC exported to CDOM from 1% to 2% and increases from 84% to 109% when doubling the tDOC exported to CDOM from 2% to 4%. The median of $a_{CDOM}[\lambda]$ is 0.08 ± 0.26 and 0.03 ± 0.25 m⁻¹ for in-situ and satellite observations, respectively. With 4% and 2% of tDOC forcing the CDOM pool, the simulated median of $a_{CDOM}[\lambda]$ is respectively fourfold (and doubled compared to observations). The simulated median is closer to observations when forcing with 1% of riverine tDOC. Comparing the time-mean 2009 CDOM absorption in the Mackenzie River plume region (Figure B1), the model forced with 2% of tDOC best fits the satellite data within the river plume area, while the model forced with 1% of tDOC results in a consistent underestimate. According to metrics and the comparison of time-mean $a_{CDOM}[\lambda]$ fields, parameterization b. was selected as the method best able to reproduce observed CDOM in the Mackenzie River plume region.

Table B1. Comparison metrics between simulated and observed $a_{CDOM}[\lambda]$ (m⁻¹

CDOM forcing parameterization	Observations	n	r	MPE	URMSE	$Median_{obs} \pm std$	$Median_{mod} \pm std$
1% of tDOC	Malina	18	0.78	45.10	0.18	0.08 ± 0.26	0.10 ± 0.14
	AMODIS	15,250	0.65	101.73	0.20	0.03 ± 0.25	0.06 ± 0.10
2% of tDOC	Malina	18	0.78	76.00	0.18	0.08 ± 0.26	0.16 ± 0.28
	AMODIS	15,250	0.65	192.06	0.19	0.03 ± 0.25	0.08 ± 0.20
4% of tDOC	Malina	18	0.79	159.20	0.39	0.08 ± 0.26	0.30 ± 0.56
	AMODIS	15,250	0.65	353.57	0.31	0.03 ± 0.25	0.14 ± 0.41

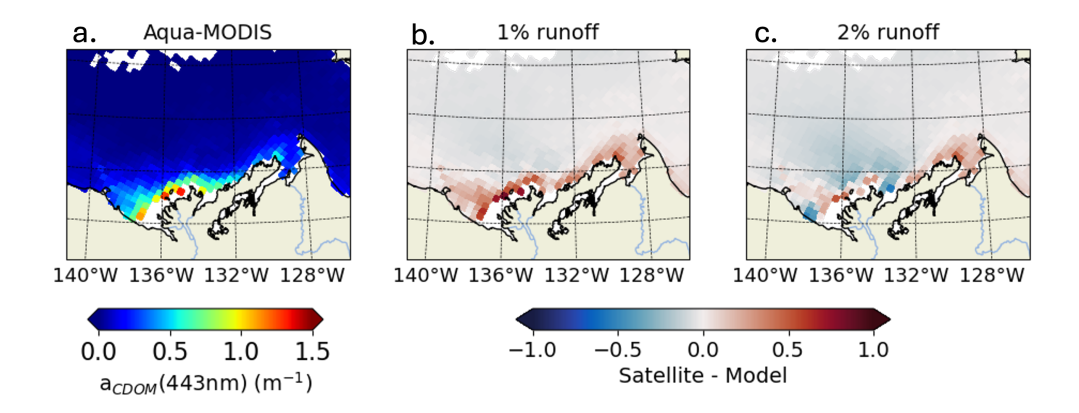


Figure B1. 2009 annual-mean CDOM absorption at 443 nm from (a) remotely-sensed observations and differences from simulated CDOM fields with (b) 1% and (c) 2% of tDOC redistributed into CDOM tracer. Simulated CDOM absorption is compared with satellite observations that are space-time colocated with the simulations.

Appendix C: sea ice phenology parameters

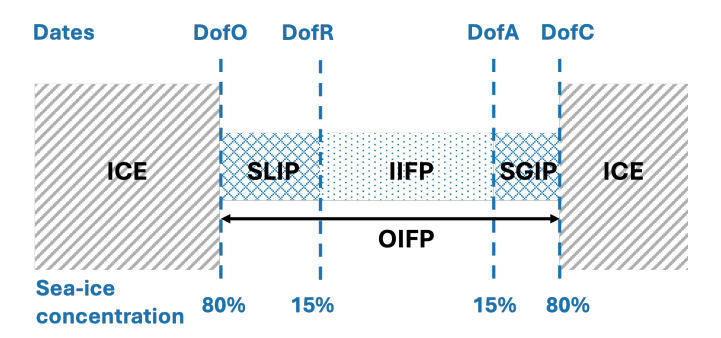


Figure C1. Conceptual diagram of sea ice seasonal evolution from spring/summer retreat (left) through fall/winter advance (right). Adapted from Bliss et al. (2019)

Appendix D: Comparison with observations

We compared the 2012 weekly surface-ocean Chla (mg Chla m $^{-3}$) and daily primary production (mg C m $^{-2}$ d $^{-1}$) simulated by ED-SBS (Run_{ctrl} and Run_{full}) with satellite observations from Lewis et al. (2020) data estimated by the AOReg.emp algorithm. We also compared simulated daily-mean SST ($^{\circ}$ C) for 2012 in both models with in-situ/satellite observations (OSTIA Good et al., 2020). As both observational products have a finer horizontal grid-spacingcompared to ED-SBS, we bin averaged the observations within each model grid cell. We then calculated the spatially-averaged value within the Mackenzie River plume region where satellite data were available to assess the model's ability to represent these observations (Figure 9 andD1). Note that the number of observations (n) available within the river plume area (n_{max}=281 for the entire area) varies in time. As both observational products provide sea ice concentration data, we also calculated observed sea ice phenology metrics to compare with our model simulations. Note that satellite observations from Lewis et al. (2020) AOReg.emp algorithm are the most suitable for model-observation comparison in the Mackenzie river plume; as they improve CDOM pollution removal in Chla estimates, using different fits of the Chla/R_{RS} (remote sensing reflectance) relationship for offshore region and shelf seas (where isobath < 1000 m). However, the Beaufort Shelf being shorter than other Arctic Seas, the Mackenzie River plume spreads out further away from the Shelf. We then observed abrupt increase in Lewis et al. (2020) Chla estimates along the shelf (1000 m isobath) due to the change in regional Chla/R_{RS} fit (see Figure S3) and decided to remove offshore data from the comparison. This only affecting a small portion of the Northwestern plume region.

ED-SBS generally represents the spatially-averaged SST amplitude and variability in the Mackenzie River plume region during the open-water period compared to observations (Figure 9c.). The model underestimates SST by 25% from mid-July to mid-September when CDOM is not included (Run_{ctrl}). Adding CDOM effects improves simulated SST by decreasing this underestimate to 17% over the same period. However, similar to phytoplankton, we observe a delay in the surface-ocean heating, which is linked to later simulated SLIP. In the observations, SST starts increasing halfway through the melting season (Figure 9c., orange line and grey area). In both simulations, SST also increases halfway through the melting season (Figure 9c., purple and grey lines and blue area), but the SLIP occurs later in the season and thus surface-ocean warming also occurs later. We observe that this difference in June SST warming manifests mainly in the northwestern section of the plume where observed sea ice melting occurs first (not shown). Simulated sea ice first melts in the eastern section of the plume and propagates westward triggering a substantial difference in northwestern plume SST throughout the season compared to observations (Figure D1a,b,c). However, the simulated eastern plume SST is comparable to observation improving by 13% the correlation coefficient in the Mackenzie river plume. This confirms that sea ice plays an important role in the ability of ED-SBS to represent physics and biogeochemistry during the spring period.

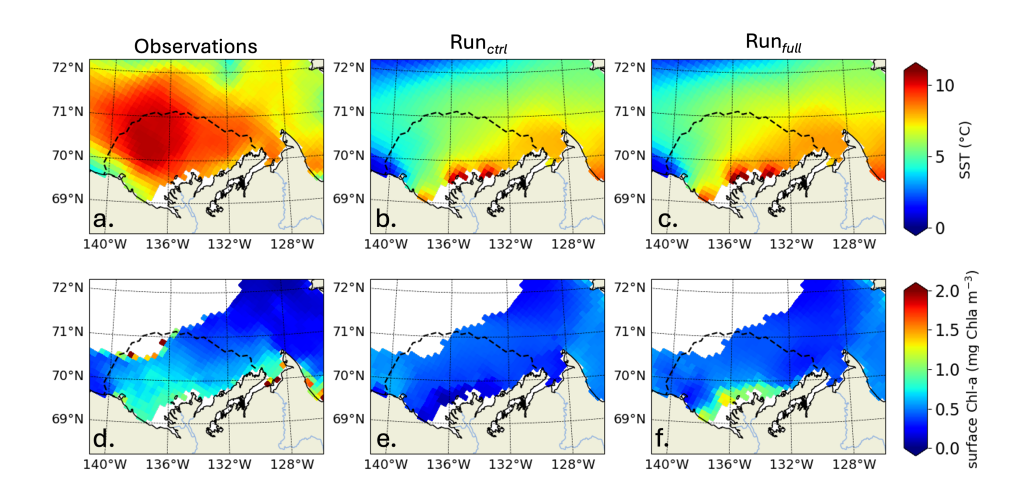


Figure D1. SST ($^{\circ}$ C) averaged from July to September 2012 (top row) and Surface Chla (mg Chla m^{-3}) averaged from June to July 2012 (lower row) for observations (a and d), $\operatorname{Run}_{ctrl}$ (c and e), $\operatorname{Run}_{full}$ (c and f). the dotted line shows the plume region; time-mean SSS isohaline of 27.

Appendix E: Phytoplankton limitation factors

555

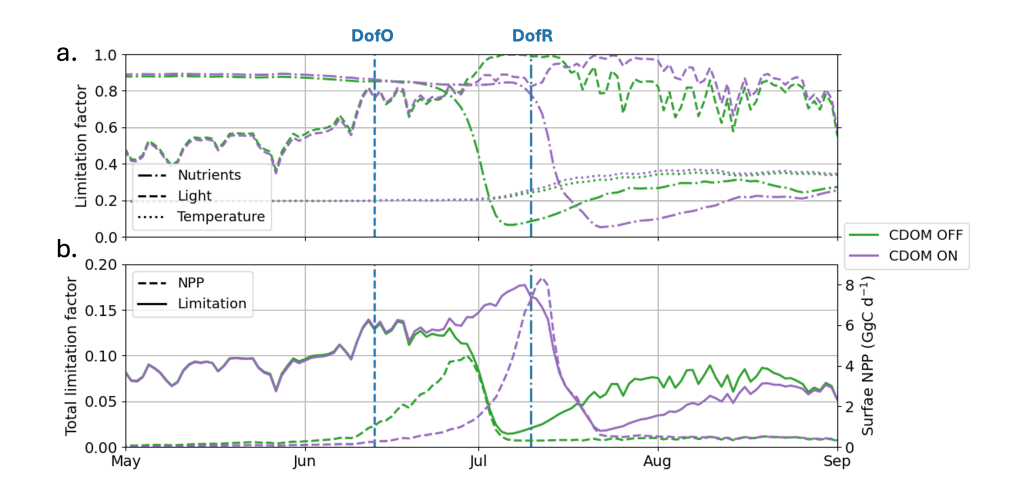


Figure E1. Simulated limitation factors for nutrients (solid lines), light (dashed lines), and temperature (dash-dotted lines), averaged between the two phytoplankton functional types and in the plume region for Run_{ctrl} (green lines) and Run_{full} (purple lines).

In ED-SBS, phytoplankton growth for each species (j) is limited by light, temperature, and nutrient availability. The three limitation factors (equations E1, E2, and E3), which yield values between 0 and 1, are combined (multiplied) to provide the total phytoplankton limitation factor. In this study, we average both phytoplankton type limitation factors in the plume region (Figure E1) to analyze the parameters affecting phytoplankton growth.

The factor with the lowest value is generally considered as the factor limiting phytoplankton growth. In the Arctic Ocean, as ocean temperatures are typically low, temperature is a consistent limitation factor year-round, shaping the background state of phytoplankton growth. In the SBS, the temperature limitation factor (γ^{temp} ; dashed dotted lines in Figure E1) in the the plume region ranges from 0.2 in winter to 0.4 during the open-water season. This seasonal change is mainly due to increased light penetration as a result of melting of sea ice and mixing of Mackenzie River-derived freshwater into the coastal ocean. The inclusion of CDOM heating has a limited influence on phytoplankton limitation. Therefore, in this study temperature limitation drives a consistent dampening effect in phytoplankton growth but does not influence phytoplankton phenology.

In winter, elevated sea ice cover causes high light limitation, with the spatially-averaged factor ranging between 0.4–0.6 in the plume region (Figure E1). Additionally, nutrients concentrations are high (see Figure 7), with a nutrient limitation factor over 0.8. Therefore, phytoplankton growth is limited by physics (both light and temperature). As sea ice begins to melt and break up (DofO), the light limitation factor increases up to 0.8 - 0.8 - 0.8 - 0.8 - 0.02 in the light limitation occurs between the simulations with 0.8 - 0.08 - 0.02 in the light limitation occurs between the simulations with 0.08 - 0.08 - 0.02 in the light limitation occurs between the simulations with 0.08 - 0.08 - 0.08 in the plume region, a difference of 0.08 - 0.02 in the light limitation occurs

slight difference in phytoplankton growth at this time, which allows the bloom to initiate in Run_{ctrl} (green dotted line; Figure E1b.) and thus delays the phytoplankton bloom by two weeks. In both simulation, elevated phytoplankton growth (mid-June or early July for Run_{ctrl} and Run_{full} , respectively) consumes nutrients, rapidly decreasing the nutrient limitation factor to ~ 0 and arresting the phytoplankton bloom. Therefore, as the nutrient limitation factor exceeds the temperature limitation factor (on July 3rd and July 15th without and with CDOM, respectively), the phytoplankton growth becomes primarily limited by nutrients. Analyzing each nutrient's (nitrate, phosphate, and silicate) limitation factor (not shown), we find that nitrate is the primarily limiting nutrient in the plume region.

560

565

In ED-SBS, the limitation factors for light (Equation E1), temperature (Equation E2), and nutrients (Equation E3) are computed using the following equations:

$$\begin{cases} \gamma_j^{light} = 1 - \exp\left(\frac{\langle \alpha I \rangle_j Chla: C_j}{P_j^{Cm}}\right) & \text{if } I_{tot} > I_{min} \\ \gamma_j^{light} = 0 & \text{else}, \end{cases}$$
(E1)

where I_{tot} and I_{min} are the total and minimum light intensity for phytoplankton growth (W m⁻²), respectively, α is the Chla specific initial slope of the photosynthesis-light curve for each species, $Chla:C_j$ is the maximum Chla carbon ratio for each species, and P_j^{Cm} is the maximum growth rate.

$$\gamma_j^{temp} = c^{Arr} \left[e^{A_e^{Ar} ((T+273.15) - T_{ref}^{Ar^{-1}}) e^{-e_{2j|T-T_j^{opt}|^{p_j}}}} \right]_{>10^{-10}}, \tag{E2}$$

where T is the ocean temperature; c^{Arr} , A_e^{Ar} and T_{ref}^{Ar} the pseudo-Arrenhius equation coefficients set to 0.5882, -4000K, and 293.15K, respectively, and T_j^{opt} is the optimal phytoplankton temperature for each species.

The nutrient limitation factor takes the value of the most limiting factor between Phosphorus, Nitrogen, Silicate and Iron:

$$\gamma_{j}^{nut} = min(\gamma_{j}^{P}, \gamma_{j}^{N}, \gamma_{j}^{Si}, \gamma_{j}^{Fe}) \text{ and } \gamma_{j}^{N} = [\gamma_{j}^{NO_{3}} + \gamma_{j}^{NO_{2}} + \gamma_{j}^{NH_{4}}]_{0}^{1}$$
 (E3)

As nitrate is the primary limiting nutrient in this study, we describe below the nitrate limitation factor:

$$\gamma_j^{N0_3} = \frac{N0_3}{N0_3 + k_j^{N0_3}} e^{-\sigma_j^{amm} NH_4},\tag{E4}$$

where $k_j^{N0_3}$ is the half-saturation concentration for nitrate limitation and $\sigma_j^{amm}NH_4$ is the coefficient for NH_4 inhibition of $N0_3$ uptake.

Code and data availability. Model code and platform-independent instructions for running ED-SBS simulations are available at https://github.com/MITgcm-contrib/ecco_darwin/tree/master/regions/mac_delta/llc270/biogeochem_setup/carroll_2020_ecosystem/CDOM_setup. Model output from all simulations described in this study (Run_{ctrl}, Run_{full}, Run_{light}, Run_{noriv}, and Run_{lin}) are available on the ECCO Drive: https://ecco.jpl.nasa.gov/drive/files/ECCO2/LLC270/Mac_Delta/CDOMsetup. ED-SBS forcing files are also available on the ECCO Drive at https://ecco.jpl.nasa.gov/drive/files/ECCO2/LLC270/Mac_Delta. Note that to access the ECCO Drive files users must register for a free Earthdata account at https://urs.earthdata.nasa.gov/users/new.

Author contributions. Conceptualization: CB, DC, DM and VLF. Methodology: CB, DC, DM and SD. Formal analysis: CB and VLF. Software: CB. Supervision: VLF, DM and CM. Funding acquisition: VLF, DM and CM. Writing – original draft preparation: CB. Writing – review and editing: CB, VLF, DC, SD, DM, AM, MM and CM.

Competing interests. The contact author has declared that none of the authors has any competing interests.

585

595

600

Acknowledgements. We would like to thanks Svetlana N. Losa for her kind collaboration and for providing us the output from Pefanis et al. (2020) simulations. CB was supported by a postdoctoral fellowship at the NASA Jet Propulsion Laboratory (JPL). A portion of this work was carried out at the Jet Propulsion Laboratory, California Institute of Technology, under a contract with the National Aeronautics and Space Administration (80NM0018D0004), with support from the Carbon Cycle Science (CCS) and Interdisciplinary Research in Earth Science (IDS) programs. DC acknowledges support from the NASA Carbon Monitoring System (CMS) program. This work is also part of the Nunataryuk project; the project has received funding under the European Union's Horizon 2020 Research and Innovation Program under grant agreement no.773421. This work was also funded by the Centre National de la Recherche Scientifique (CNRS, LEFE program). Part of this research was supported by Japan Aerospace Exploration Agency (JAXA) Global Change Observation Mission-Climate (GCOM-C) to AM (contract #23RT000390). © 2025. All rights reserved.

References

610

- Aarnos, H., Gélinas, Y., Kasurinen, V., Gu, Y., Puupponen, V., and Vähätalo, A. V.: Photochemical mineralization of terrigenous DOC to dissolved inorganic carbon in ocean, Global Biogeochemical Cycles, 32, 250–266, https://doi.org/10.1002/2017GB005698, 2018.
- Ardyna, M. and Arrigo, K.: Phytoplankton dynamics in a changing Arctic Ocean, Nature Climate Change, 10, 892–903, https://doi.org/10.1038/s41558-020-0905-y, 2020.
 - Arrigo, K. and Van Dijken, G.: Continued increases in Arctic Ocean primary production, Progress in oceanography, 136, 60–70, https://doi.org/10.1016/j.pocean.2015.05.002, 2015.
 - Arrigo, K., Matrai, P., and Van Dijken, G.: Primary productivity in the Arctic Ocean: Impacts of complex optical properties and subsurface chlorophyll maxima on large-scale estimates, Journal of Geophysical Research: Oceans, 116, https://doi.org/10.1029/2011JC007273, 2011.
 - Bélanger, S., Xie, H., Krotkov, N., Larouche, P., Vincent, W., and Babin, M.: Photomineralization of terrigenous dissolved organic matter in Arctic coastal waters from 1979 to 2003: Interannual variability and implications of climate change, Global Biogeochemical Cycles, 20, https://doi.org/10.1029/2006GB002708, 2006.
- Bélanger, S., Babin, M., and Tremblay, J.-É.: Increasing cloudiness in Arctic damps the increase in phytoplankton primary production due to sea ice receding, Biogeosciences, 10, 4087–4101, https://doi.org/10.5194/bg-10-4087-2013, 2013.
 - Berezovski, A., Hessen, D., and Andersen, T.: Photon budgets and the relative effects of CDOM and pigment absorptions on primary production along a coastal salinity gradient, Frontiers in Photobiology, 2, 1452 747, https://doi.org/10.3389/fphbi.2024.1452747, 2025.
 - Bertin, C., Matsuoka, A., Mangin, A., Babin, M., and Le Fouest, V.: Merging Satellite and *in situ* Data to Assess the Flux of Terrestrial Dissolved Organic Carbon From the Mackenzie River to the Coastal Beaufort Sea, Frontiers in Earth Science, 10, https://doi.org/10.3389/feart.2022.694062, 2022.
 - Bertin, C., Carroll, D., Menemenlis, D., Dutkiewicz, S., Zhang, H., Matsuoka, A., Tank, S., Manizza, M., Miller, C., Babin, M., Mangin, A., and Le Fouest, V.: Biogeochemical river runoff drives intense coastal Arctic Ocean CO₂ outgassing, Geophysical Research Letters, 50, e2022GL102377, https://doi.org/10.1029/2022GL102377, 2023.
- Bertin, C., Carroll, D., Menemenlis, D., Dutkiewicz, S., Zhang, H., Schwab, M., Savelli, R., Matsuoka, A., Manizza, M., Miller, C., Bowring,
 S., Guenet, B., and Le Fouest, V.: Paving the way for improved representation of coupled physical and biogeochemical processes in Arctic
 River plumes A case study of the Mackenzie Shelf, Permafrost and Periglicial Processes, https://doi.org/10.1002/ppp.2271, 2025.
 - Bliss, A., Steele, M., Peng, G., Meier, W., and Dickinson, S.: Regional variability of Arctic sea ice seasonal change climate indicators from a passive microwave climate data record, Environmental Research Letters, 14, 045 003, https://doi.org/10.1088/1748-9326/aafb84, 2019.
- Blough, N. V. and Del Vecchio, R.: Chromophoric DOM in the coastal environment, Biogeochemistry of marine dissolved organic matter, https://doi.org/10.1016/B978-012323841-2/50012-9, 2002.
 - Brix, H., Menemenlis, D., Hill, C., Dutkiewicz, S., Jahn, O., Wang, D., Bowman, K., and Zhang, H.: Using Green's Functions to initialize and adjust a global, eddying ocean biogeochemistry general circulation model, Ocean Modelling, 95, 1–14, https://doi.org/10.1016/j.ocemod.2015.07.008, 2015.
- Carmack, E. and Macdonald, R.: Oceanography of the Canadian Shelf of the Beaufort Sea: a setting for marine life, Arctic, pp. 29–45, https://doi.org/10.1111/gcb.16815, 2002.
 - Carroll, D., Menemenlis, D., Adkins, J., Bowman, K., Brix, H., Dutkiewicz, S., Fenty, I., Gierach, M., Hill, C., Jahn, O., Landschützer, P., Lauderdale, J., Liu, J., Manizza, M., Naviaux, J., Rödenbeck, C., Schimel, D., Van der Stocken, T., and Zhang, H.: The ECCO-Darwin

- data-assimilative global ocean biogeochemistry model: Estimates of seasonal to multidecadal surface ocean pCO₂ and air–sea CO₂ flux, Journal of Advances in Modeling Earth Systems, 12, e2019MS001 888, https://doi.org/10.1029/2019MS001888, 2020.
- Carroll, D., Menemenlis, D., Dutkiewicz, S., Lauderdale, J., Adkins, J., Bowman, K., Brix, H., Fenty, I., Gierach, M., Hill, C., Jahn, O., Landschützer, P., Manizza, M., Mazloff, M., Miller, C., Schimel, D., Verdy, A., Whitt, D., and Zhang, H.: Attribution of Space-Time Variability in Global-Ocean Dissolved Inorganic Carbon, Global Biogeochemical Cycles, 36, e2021GB007162, https://doi.org/10.1029/2021GB007162, 2022.
- Choi, J., Matsuoka, A., Manizza, M., Carroll, D., Dutkiewicz, S., and Lippmann, T.: A new ecosystem model for Arctic phytoplankton phenology from ice-covered to open-water periods: Implications for future sea ice retreat scenarios, Geophysical Research Letters, 51, e2024GL110155, https://doi.org/10.1029/2024GL110155, 2024.
 - Clark, J., Mannino, A., Tzortziou, M., Spencer, R., and Hernes, P.: The transformation and export of organic carbon across an arctic river-delta-ocean continuum, Journal of Geophysical Research: Biogeosciences, 127, e2022JG007139, https://doi.org/10.1126/science.1253119, 2022.
- Clement Kinney, J., Frants, M., Maslowski, W., Osinski, R., Jeffery, N., Jin, M., and Lee, Y.: Investigation of Under-Ice Phytoplankton Growth in the Fully-Coupled, High-Resolution Regional Arctic System Model, Journal of Geophysical Research: Oceans, 128, e2022JC019 000, https://doi.org/10.1029/2022JC019000, 2023.
 - Cory, R. and Kling, G.: Interactions between sunlight and microorganisms influence dissolved organic matter degradation along the aquatic continuum, Limnology and Oceanography Letters, 3, 102–116, https://doi.org/10.1002/lol2.10060, 2018.
- 655 Cory, R., Ward, C., Crump, B., and Kling, G.: Sunlight controls water column processing of carbon in arctic fresh waters, Science, 345, 925–928, https://doi.org/10.1002/lol2.10060, 2014.
 - Dai, M., Su, J., Zhao, Y., Hofmann, E., Cao, Z., Cai, W.-J., Gan, J., Lacroix, F., Laruelle, G., Meng, F., and Wang, Z.: Carbon fluxes in the coastal ocean: synthesis, boundary processes, and future trends, Annual Review of Earth and Planetary Sciences, 50, 593–626, https://doi.org/10.1146/annurev-earth-032320-090746, 2022.
- Dittmar, T. and Kattner, G.: The biogeochemistry of the river and shelf ecosystem of the Arctic Ocean: a review, Marine chemistry, 83, 103–120, https://doi.org/10.1016/S0304-4203(03)00105-1, 2003.
 - Dittmar, T., Lennartz, S., Buck-Wiese, H., Hansell, D. A., Santinelli, C., Vanni, C., Blasius, B., and Hehemann, J.: Enigmatic persistence of dissolved organic matter in the ocean, Nature Reviews Earth & Environment, 2, 570–583, https://doi.org/10.5194/bg-12-3551-2015, 2021.
 - Doxaran, D., Devred, E., and Babin, M.: A 50% increase in the mass of terrestrial particles delivered by the Mackenzie River into the Beaufort Sea (Canadian Arctic Ocean) over the last 10 years, Biogeosciences, 12, 3551–3565, https://doi.org/10.5194/bg-12-3551-2015, 2015.

- Dutkiewicz, S., Scott, J., and Follows, M.: Winners and losers: Ecological and biogeochemical changes in a warming ocean, Global Biogeochemical Cycles, 27, 463–477, https://doi.org/10.1002/gbc.20042, 2013.
- Dutkiewicz, S., Hickman, A., Jahn, O., Gregg, W., Mouw, C., and Follows, M.: Capturing optically important constituents and properties in a marine biogeochemical and ecosystem model, Biogeosciences, 12, 4447–4481, https://doi.org/10.5194/bg-12-4447-2015, 2015.
- Dutkiewicz, S., Hickman, A., Jahn, O., Henson, S., Beaulieu, C., and Monier, E.: Ocean colour signature of climate change, Biogeosciences, 10, 578, https://doi.org/10.1038/s41467-019-08457-x, 2019.
 - Feng, D., Gleason, C., Lin, P., Yang, X., Pan, M., and Ishitsuka, Y.: Recent changes to Arctic river discharge, Nature communications, 12, 6917, https://doi.org/10.1038/s41467-021-27228-1, 2021.
- Follows, M., Ito, T., and Dutkiewicz, S.: On the solution of the carbonate chemistry system in ocean biogeochemistry models, Ocean Modelling, 12, 290–301, https://doi.org/0.1016/j.ocemod.2005.05.004, 2006.

- Follows, M., Dutkiewicz, S., Grant, S., and Chisholm, S.: Emergent biogeography of microbial communities in a model ocean, science, 315, 1843–1846, https://doi.org/10.1126/science.1138544, 2007.
- Gibson, G. A., Elliot, S., Clement Kinney, J., Piliouras, A., and Jeffery, N.: Assessing the potential impact of river chemistry on Arctic coastal production, Frontiers in Marine Science, 9, 738 363, https://doi.org/10.3389/fmars.2022.738363, 2022.
- 680 Gnanadesikan, A., Kim, G., and Pradal, M.-A.: Impact of colored dissolved materials on the annual cycle of sea surface temperature: potential implications for extreme ocean temperatures, Geophysical Research Letters, 46, 861–869, https://doi.org/10.1029/2018GL080695, 2019.
 - Good, S., Fiedler, E., Mao, C., Martin, M., Maycock, A., Reid, R., Roberts-Jones, J., Searle, T., Waters, J., While, J., and Worsfold, M.: The current configuration of the OSTIA system for operational production of foundation sea surface temperature and ice concentration analyses, Remote Sensing, 12, 720, https://doi.org/10.3390/rs12040720, 2020.
- 685 Grunert, B., Tzortziou, M., Neale, P., Menendez, A., and Hernes, P.: DOM degradation by light and microbes along the Yukon River-coastal ocean continuum, Scientific Reports, 11, 10 236, https://doi.org/10.1038/s41598-021-89327-9, 2021.
 - Hill, V.: Impacts of chromophoric dissolved organic material on surface ocean heating in the Chukchi Sea, Journal of Geophysical Research: Oceans, 113, https://doi.org/10.1029/2007JC004119, 2008.
- Holmes, R., McClelland, J., Raymond, P., Frazer, B., Peterson, B., and Stieglitz, M.: Lability of DOC transported by Alaskan rivers to the Arctic Ocean, Geophysical Research Letters, 35, https://doi.org/10.1029/2007GL032837, 2008.
 - IPCC: Climate Change 2023: Synthesis Report. Contribution of Working Groups I, II and III to the Sixth Assessment Report of the Intergovernmental Panel on Climate Change., chap. Section 2: Current Status and Trends, pp. 35–115, IPCC, Geneva, Switzerland, Core Writing Team and Lee, H. and Romero, J. edn., https://doi.org/10.59327/IPCC/AR6-9789291691647, 2023.
- Juhls, B., Matsuoka, A., Lizotte, M., Bécu, G., Overduin, P., El Kassar, J., Devred, E., Doxaran, D., Ferland, J., Forget, M., Ferland, J., Forget,
 M., Hilborn, A., Hieronymi, M., Leymarie, E., Maury, J., Oziel, L., Tisserand, L., Anikina, D., Dillon, M., and Babin, M.: Seasonal dynamics of dissolved organic matter in the Mackenzie Delta, Canadian Arctic waters: Implications for ocean colour remote sensing,
 Remote Sensing of Environment, 283, 113 327, https://doi.org/10.1016/j.rse.2022.113327, 2022.
 - Kim, G., Gnanadesikan, A., and Pradal, M.-A.: Increased surface ocean heating by colored detrital matter (CDM) linked to greater Northern Hemisphere ice formation in the GFDL CM2Mc ESM, Journal of Climate, 29, 9063–9076, https://doi.org/10.1175/JCLI-D-16-0053.1, 2016.

- Kim, G., Gnanadesikan, A., Del Castillo, C., and Pradal, M.-A.: Upper ocean cooling in a coupled climate model due to light attenuation by yellowing materials, Geophysical research letters, 45, 6134–6140, https://doi.org/10.1029/2018GL077297, 2018.
- Lacroix, F., Ilyina, T., Mathis, M., Laruelle, G. G., and Regnier, P.: Historical increases in land-derived nutrient inputs may alleviate effects of a changing physical climate on the oceanic carbon cycle, Global change biology, 27, 5491–5513, https://doi.org/10.1111/gcb.15822, 2021.
- Le Fouest, V., Babin, M., and Tremblay, J.-É.: The fate of riverine nutrients on Arctic shelves, Biogeosciences, 10, 3661–3677, https://doi.org/10.5194/bg-10-3661-2013, 2013.
- Lengaigne, M., Madec, G., Bopp, L., Menkes, C., Aumont, O., and Cadule, P.: Bio-physical feedbacks in the Arctic Ocean using an Earth system model, Geophysical Research Letters, 36, https://doi.org/10.1029/2009GL040145, 2009.
- Lewis, K. and Arrigo, K.: Ocean color algorithms for estimating chlorophyll a, CDOM absorption, and particle backscattering in the Arctic Ocean, Journal of Geophysical Research: Oceans, 125, e2019JC015 706, https://doi.org/10.1029/2019JC015706, 2020.
 - Lewis, K., Van Dijken, G., and Arrigo, K.: Changes in phytoplankton concentration now drive increased Arctic Ocean primary production, Science, 369, 198–202, https://doi.org/10.1126/science.aay8380, 2020.

- Li, J., Matsuoka, A., Pang, X., Massicotte, P., and Babin, M.: Performance of Algorithms for Retrieving Chlorophyll a Concentrations in the

 Arctic Ocean: Impact on Primary Production Estimates, Remote Sensing, 16, 892, https://doi.org/10.3390/rs16050892, 2024.
 - Lizotte, M., Juhls, B., Matsuoka, A., Massicotte, P., Mével, G., Anikina, D., Antonova, S., Bécu, G., Béguin, M., Bélanger, S., et al.: Nunataryuk field campaigns: understanding the origin and fate of terrestrial organic matter in the coastal waters of the Mackenzie Delta region, Earth System Science Data, 15, 1617–1653, https://doi.org/10.5194/essd-2022-163, 2023.
- Manizza, M., Follows, M., Dutkiewicz, S., McClelland, J., Menemenlis, D., Hill, C., Townsend-Small, A., and Peterson, B.:

 Modeling transport and fate of riverine dissolved organic carbon in the Arctic Ocean, Global Biogeochemical Cycles, 23, https://doi.org/10.1029/2008GB003396, 2009.
 - Manizza, M., Menemenlis, D., Zhang, H., and Miller, C.: Modeling the recent changes in the Arctic Ocean C0₂ sink (2006–2013), Global Biogeochemical Cycles, 33, https://doi.org/10.1029/2018GB006070, 2019.
- Manizza, M., Carroll, D., Menemenlis, D., Zhang, H., and Miller, C.: Modeling the recent changes of phytoplankton blooms dynamics in the
 Arctic Ocean, Journal of Geophysical Research: Oceans, 128, https://doi.org/10.1029/2022JC019152, 2023.
 - Mann, P., Spencer, R., Hernes, P., Six, J., Aiken, G., Tank, S., McClelland, J., Butler, K., Dyda, R., and Holmes, R.: Pan-Arctic trends in terrestrial dissolved organic matter from optical measurements, Frontiers in Earth Science, 4, 25, https://doi.org/10.3389/feart.2016.00025, 2016.
- Mann, P., Strauss, J., Palmtag, J., Dowdy, K., Ogneva, O., Fuchs, M., Bedington, M., Torres, R., Polimene, L., Overduin, P., Mollenhauer,
 G., Grosse, G., Rachold, V., Sobczak, W., Spencer, R., and Juhls, B.: Degrading permafrost river catchments and their impact on Arctic Ocean nearshore processes, Ambio, 51, 439–455, https://doi.org/10.1007/s13280-021-01666-z, 2022.
 - Massicotte, P., Amon, R. M., Antoine, D., Archambault, P., Balzano, S., Bélanger, S., Benner, R., Boeuf, D., Bricaud, A., Bruyant, F., and Babin, M.: The MALINA oceanographic expedition: how do changes in ice cover, permafrost and UV radiation impact biodiversity and biogeochemical fluxes in the Arctic Ocean?, Earth System Science Data, 13, 1561–1592, https://doi.org/10.5194/essd-2020-252, 2021.
- Mathis, M., Logemann, K., Maerz, J., Lacroix, F., Hagemann, S., Chegini, F., Ramme, L., Ilyina, T., Korn, P., and Schrum, C.: Seamless integration of the coastal ocean in global marine carbon cycle modeling, Journal of Advances in Modeling Earth Systems, 14, e2021MS002789, https://doi.org/10.1029/2021MS002789, 2022.

- Matsuoka, A., Bricaud, A., Benner, R., Para, J., Sempéré, R., Prieur, L., Bélanger, S., and Babin, M.: Tracing the transport of colored dissolved organic matter in water masses of the Southern Beaufort Sea: relationship with hydrographic characteristics, Biogeosciences, 9, 925–940, https://doi.org/10.5194/bg-9-925-2012, 2012.
- Matsuoka, A., Babin, M., and Devred, E.: A new algorithm for discriminating water sources from space: A case study for the southern Beaufort Sea using MODIS ocean color and SMOS salinity data, Remote Sensing of Environment, 184, 124–138, https://doi.org/10.1016/j.rse.2016.05.006, 2016.
- Matsuoka, A., Boss, E., Babin, M., Karp-Boss, L., Hafez, M., Chekalyuk, A., Proctor, C. W., Werdell, P. J., and Bricaud, A.: Pan-Arctic optical characteristics of colored dissolved organic matter: Tracing dissolved organic carbon in changing Arctic waters using satellite ocean color data, Remote sensing of Environment, 200, 89–101, https://doi.org/10.1016/j.rse.2017.08.009, 2017.
 - McClelland, J., Holmes, R., Dunton, K., and Macdonald, R.: The Arctic ocean estuary, Estuaries and Coasts, 35, 353–368, https://doi.org/10.1007/s12237-010-9357-3, 2012.
- McClelland, J., Holmes, R., Peterson, B., Raymond, P., Striegl, R., Zhulidov, A., Zimov, S., Zimov, N., Tank, S., Spencer, R., Staples, R., Gurtovaya, T., and Griffin, C.: Particulate organic carbon and nitrogen export from major Arctic rivers, Global Biogeochemical Cycles, 30, 629–643, https://doi.org/10.1002/2015GB005351, 2016.

- McClelland, J., Tank, S., Shiklomanov, A., Spencer, R., Zolkos, S., and Holmes, R.: ArcticGRO Discharge Dataset, WebPage: https://arcticgreatrivers.org/data/, Accessed: 2023-03-07, 2023.
- Morley, J.: Observations of flow distributions and river breakup in the Mackenzie Delta, NWT, Master's thesis, University of Alberta, Alberta, 755 Canada, https://doi.org/10.7939/R3N02H, 2012.
 - Nadaï, G., Nöthig, E.-M., Fortier, L., and Lalande, C.: Early snowmelt and sea ice breakup enhance algal export in the Beaufort Sea, Progress in Oceanography, 190, 102 479, https://doi.org/10.1016/j.pocean.2020.102479, 2021.
 - Neumann, T., Siegel, H., Moros, M., Gerth, M., Kniebusch, M., and Heydebreck, D.: Ventilation of the northern Baltic Sea, Ocean Science, 16, 767–780, https://doi.org/10.5194/os-16-767-2020, 2020.
- Neumann, T., Koponen, S., Attila, J., Brockmann, C., Kallio, K., Kervinen, M., Mazeran, C., Müller, D., Philipson, P., Thulin, S., Väkevä, S., and Ylöstalo, P.: Optical model for the Baltic Sea with an explicit CDOM state variable: a case study with Model ERGOM (version 1.2), Geoscientific Model Development, 14, 5049–5062, https://doi.org/10.5194/gmd-14-5049-2021, 2021.

- Nguyen, H., Lee, Y., Hong, J., Hong, S., Chen, M., and Hur, J.: Climate warming-driven changes in the flux of dissolved organic matter and its effects on bacterial communities in the Arctic Ocean: a review, Frontiers in Marine Science, 9, 968 583, https://doi.org/10.3389/fmars.2022.968583, 2022.
- Nielsen, D., Pieper, P., Barkhordarian, A., Overduin, P., Ilyina, T., Brovkin, V., Baehr, J., and Dobrynin, M.: Increase in Arctic coastal erosion and its sensitivity to warming in the twenty-first century, Nature Climate Change, 12, 263–270, https://doi.org/10.1038/s41558-022-01281-0, 2022.
- Nielsen, D., Chegini, F., Maerz, J., Brune, S., Mathis, M., Dobrynin, M., Baehr, J., Brovkin, V., and Ilyina, T.: Reduced Arctic Ocean CO₂ uptake due to coastal permafrost erosion, Nature Climate Change, pp. 1–8, https://doi.org/10.1038/s41558-024-02074-3, 2024.
- Osburn, C., Retamal, L., and Vincent, W.: Photoreactivity of chromophoric dissolved organic matter transported by the Mackenzie River to the Beaufort Sea, Marine Chemistry, 115, 10–20, https://doi.org/10.1016/j.marchem.2009.05.003, 2009.
- Parkinson, C. and Comiso, J.: On the 2012 record low Arctic sea ice cover: Combined impact of preconditioning and an August storm, Geophysical Research Letters, 40, 1356–1361, https://doi.org/10.1002/grl.50349, 2013.
- Paulson, C. and Simpson, J.: Irradiance measurements in the upper ocean, Journal of Physical Oceanography, 7, 952–956, https://doi.org/10.1175/1520-0485(1977)007<0952:IMITUO>2.0.CO;2, 1977.
 - Pefanis, V., Losa, S., Losch, M., Janout, M. A., and Bracher, A.: Amplified Arctic surface warming and sea ice loss due to phytoplankton and colored dissolved material, Geophysical Research Letters, 47, e2020GL088795, https://doi.org/10.1029/2020GL088795, 2020.
- Rantanen, M., Karpechko, A., Lipponen, A., Nordling, K., Hyvärinen, O., Ruosteenoja, K., Vihma, T., and Laaksonen, A.: The Arctic has warmed nearly four times faster than the globe since 1979, Communications earth & environment, 3, 168, https://doi.org/10.1038/s43247-022-00498-3, 2022.
 - Roobaert, A., Laruelle, G., Landschützer, P., Gruber, N., Chou, L., and Regnier, P.: The spatiotemporal dynamics of the sources and sinks of CO₂ in the global coastal ocean, Global Biogeochemical Cycles, 33, 1693–1714, https://doi.org/10.1029/2019GB006239, 2019.
- Roobaert, A., Resplandy, L., Laruelle, G. G., Liao, E., and Regnier, P.: Unraveling the physical and biological controls of the global coastal CO₂ sink, Global Biogeochemical Cycles, 38, e2023GB007799, https://doi.org/10.1029/2023GB007799, 2024.
 - Sauerland, L., Ray, N., Martens, J., Tesi, T., Dudarev, O., Gustafsson, Ö., Semiletov, I., and Wild, B.: Terrestrial organic matter contributes to CO₂ production from Siberian shelf sediments, Journal of Geophysical Research: Biogeosciences, 130, e2024JG008226, https://doi.org/10.1029/2024JG008226, 2025.

- Savelli, R., Carroll, D., Menemenlis, D., Lauderdale, J., Bertin, C., Dutkiewicz, S., Manizza, M., Bloom, A., Castro-Morales, K., Miller, C., Simard, M., Bowman, K., and Zhang, H.: Implementing Riverine Biogeochemical Inputs in ECCO-Darwin: a Critical Step Forward for a Pioneering Data-Assimilative Global-Ocean Biogeochemistry Model, EGUsphere, 2025, 1–30, https://doi.org/10.5194/egusphere-2025-1707, 2025.
 - Silsbe, G., Behrenfeld, M., Halsey, K., Milligan, A., and Westberry, T.: The CAFE model: A net production model for global ocean phytoplankton, Global Biogeochemical Cycles, 30, 1756–1777, https://doi.org/10.1002/2016GB005521, 2016.
- Soppa, M., Pefanis, V., Hellmann, S., Losa, S., Hölemann, J., Martynov, F., Heim, B., Janout, M. A., Dinter, T., Rozanov, V., and Bracher, A.: Assessing the influence of water constituents on the radiative heating of Laptev Sea shelf waters, Frontiers in Marine Science, 6, 221, https://doi.org/10.3389/fmars.2019.00221, 2019.

- Spencer, R., Aiken, G., Butler, K., Dornblaser, M., Striegl, R., and Hernes, P.: Utilizing chromophoric dissolved organic matter measurements to derive export and reactivity of dissolved organic carbon exported to the Arctic Ocean: A case study of the Yukon River, Alaska, Geophysical Research Letters, 36, https://doi.org/10.1029/2008GL036831, 2009.
- Spencer, R., Mann, P., Dittmar, T., Eglinton, T., McIntyre, C., Holmes, R., Zimov, N., and Stubbins, A.: Detecting the signature of permafrost thaw in Arctic rivers, Geophysical Research Letters, 42, 2830–2835, https://doi.org/10.1002/2015GL063498, 2015.
- Stedmon, C., Amon, R., Rinehart, A., and Walker, S.: The supply and characteristics of colored dissolved organic matter (CDOM) in the Arctic Ocean: Pan Arctic trends and differences, Marine Chemistry, 124, 108–118, https://doi.org/10.1016/j.marchem.2010.12.007, 2011.
- Stramski, D., Boss, E., Bogucki, D., and Voss, K.: The role of seawater constituents in light backscattering in the ocean, Progress in Oceanography, 61, 27–56, https://doi.org/10.1016/j.pocean.2004.07.001, 2004.
 - Sulpis, O., Humphreys, M., Wilhelmus, M., Carroll, D., Berelson, W., Menemenlis, D., Middelburg, J., and Adkins, J.: RADIv1: a non-steady-state early diagenetic model for ocean sediments in Julia and MATLAB/GNU Octave, Geoscientific Model Development, 15, 2105–2131, https://doi.org/10.5194/gmd-15-2105-2022, 2022.
- Tank, S., McClelland, J., Spencer, R., Shiklomanov, A., Suslova, A., Moatar, F., Amon, R., Cooper, L., Elias, G., Gordeev, V., Guay, C., Gurtovaya, T., Kosmenko, L., Mutter, E., Peterson, B., Peucker-Ehrenbrink, B., Raymond, P., Schuster, P., Scott, L., Staples, R., Striegl, R., Tretiakov, M., Zhulidov, A., Zimov, N., Zimov, S., and Holmes, R.: Recent trends in the chemistry of major northern rivers signal widespread Arctic change, Nature Geoscience, 16, 789–796, https://doi.org/10.1038/s41561-023-01247-7, 2023.
- Tanski, G., Bröder, L., Wagner, D., Knoblauch, C., Lantuit, H., Beer, C., Sachs, T., Fritz, M., Tesi, T., Koch, B., Haghipour, N., Eglinton, T.,
 Strauss, J., and Vonk, J.: Permafrost carbon and CO₂ pathways differ at contrasting coastal erosion sites in the Canadian Arctic, Frontiers in Earth Science, 9, 630 493, https://doi.org/10.3389/feart.2021.630493, 2021.
 - Terhaar, J., Orr, J., Ethé, C., Regnier, P., and Bopp, L.: Simulated Arctic Ocean response to doubling of riverine carbon and nutrient delivery, Global Biogeochemical Cycles, 33, 1048–1070, https://doi.org/10.1038/s41467-020-20470-z, 2019.
- Terhaar, J., Lauerwald, R., Regnier, P., Gruber, N., and Bopp, L.: Around one third of current Arctic Ocean primary production sustained by rivers and coastal erosion, Nature Communications, 12, 169, https://doi.org/10.1029/2019GB006200, 2021.
 - Tisserand, L., Lizotte, M., Forget, M.-H., Lozano, J.-C., Matsuoka, A., Stedmon, C., Babin, M., and Joux, F.: Degradation of terrigenous dissolved organic matter in Arctic coastal waters: Importance of the priming effect and identification of microbials actors, Sentinel North Scientific Meeting, November 2-4, 2021, https://issuu.com/sn683/docs/rssn2021_proceedings_resumes?fr=sNzEzNDQzNDQ5OTE, 2021.
- Tokuda, D., Kim, H., Yamazaki, D., and Oki, T.: Development of a global river water temperature model considering fluvial dynamics and seasonal freeze-thaw cycle, Water Resources Research, 55, 1366–1383, https://doi.org/10.1029/2018WR023083, 2019.

- U.S. D.O.E.: ASTM G173-03 Reference Spectra Derived from SMARTS v. 2.9.2. U.S. Department of Energy (DOE)/NREL/ALLIANCEP, https://www.nrel.gov/grid/solar-resource/spectra-am1.5.html, Accessed: 2024-06-05, 2005.
- Ward, C., Nalven, S., Crump, B., Kling, G., and Cory, R.: Photochemical alteration of organic carbon draining permafrost soils shifts microbial metabolic pathways and stimulates respiration, Nature communications, 8, 772, https://doi.org/10.1038/s41467-017-00759-2, 2017.

- Wozniak, B. and Dera, J.: Light Absorption by Suspended Particulate Matter (SPM) in Sea Water, pp. 167–294, Springer New York, New York, NY, ISBN 978-0-387-49560-6, https://doi.org/10.1007/978-0-387-49560-6_5, 2007.
- Yasunaka, S., Manizza, M., Terhaar, J., Olsen, A., Yamaguchi, R., Landschützer, P., Watanabe, E., Carroll, D., Adiwira, H., Müller, J., and Hauck, J.: An assessment of CO₂ uptake in the Arctic Ocean from 1985 to 2018, Global Biogeochemical Cycles, 37, e2023GB007 806, https://doi.org/10.22541/essoar.168476524.42265823/v1, 2023.
- Zhang, H., Menemenlis, D., and Fenty, I.: ECCO LLC270 ocean-ice state estimate, Tech. rep., Jet Propulsion Laboratory, California Institute of Technology, Pasadena, CA, 2018.